Published for SISSA by Springer

Received: May 14, 2018
Accepted: June 30, 2018
Published: July 13, 2018

Radiative bound-state formation in unbroken perturbative non-Abelian theories and implications for dark matter

Julia Harz[a] **and Kalliopi Petraki**[a,b]

[a] *Laboratoire de Physique Théorique et Hautes Energies (LPTHE), UMR 7589 CNRS & Sorbonne Université, 4 Place Jussieu, F-75252, Paris, France*
[b] *Nikhef, Science Park 105, 1098 XG Amsterdam, The Netherlands*

E-mail: jharz@lpthe.jussieu.fr, kpetraki@lpthe.jussieu.fr

Abstract: We compute the cross-sections for the radiative capture of non-relativistic particles into bound states, in unbroken perturbative non-Abelian theories. We find that the formation of bound states via emission of a gauge boson can be significant for a variety of dark matter models that feature non-Abelian long-range interactions, including multi-TeV scale WIMPs, dark matter co-annihilating with coloured partners and hidden-sector models. Our results disagree with previous computations, on the relative sign of the Abelian and non-Abelian contributions. In particular, in the case of capture of a particle-antiparticle pair into its tightest bound state, we find that these contributions add up, rather than partially canceling each other. We apply our results to dark matter co-annihilating with particles transforming in the (anti)fundamental of $SU(3)_c$, as is the case in degenerate stop-neutralino scenarios in the MSSM. We show that the radiative formation and decay of particle-antiparticle bound states can deplete the dark matter density by $(40 - 240)\%$, for dark matter heavier than 500 GeV. This implies a larger mass difference between the co-annihilating particles, and allows for the dark matter to be as heavy as 3.3 TeV.

Keywords: Beyond Standard Model, Cosmology of Theories beyond the SM, Perturbative QCD

ArXiv ePrint: 1805.01200

https://doi.org/10.1007/JHEP07(2018)096

JHEP07(2018)096

Contents

JHEP07(2018)096

1 Introduction

In theories with light force mediators, the formation of bound states may have significant implications. Early work pointed out aspects of the effect of bound states on the expected dark matter (DM) detection signatures [1–3]. More recently, a variety of phenomenological implications have been identified or explored in greater depth. It has been shown that the formation and decay of unstable bound states can affect the density of thermal-relic DM [4], and is essential in determining the unitarity limit on the DM mass [5]. Moreover, bound-state formation (BSF) processes enhance the expected annihilation signals of symmetric [1, 6–11] and asymmetric DM [5, 12]. Since BSF cross-sections are typically dominated by different partial waves than the direct annihilation processes, they exhibit different velocity dependence and resonance structure, and can give rise to complementary signatures [7, 9]. In the case of asymmetric DM [13], the formation of stable bound states

may produce novel direct [14, 15] and indirect detection signals [16–19], as well as affect the DM self-scattering inside haloes [20]. In confining theories, bound states may set the DM mass scale [21, 22], and relate it to that of ordinary matter [23]. Finally, DM bound states may have implications for collider experiments [3, 24–26].[1]

Here, we consider BSF processes in non-Abelian theories. Non-Abelian interactions are particularly important in scenarios where DM is coannihilating with coloured partners, as well as in models where DM consists of TeV-scale Weakly interacting massive particles (WIMPs). Scenarios that feature DM coannihilation with coloured particles are encountered within the minimal supersymmetric standard model (MSSM) [32–39], and are in part motivated by the measurement of the Higgs mass [40, 41]. These scenarios are being probed in high-precision collider experiments; the accurate prediction of the DM density within their parameter space is therefore necessary in order for the cosmological constraints to meaningfully complement those from colliders. On the other hand, TeV-scale WIMP models are being probed mostly via indirect searches. Their annihilation signals exhibit sharp resonances that depend on the DM mass [42–46]. It follows that the precise value of the DM mass, which, under minimal assumptions, is predicted by the observed DM density, determines the viability of these models. Clearly, in both cases, an accurate computation of the DM freeze-out is necessary. It is then essential that the depletion of the DM abundance via BSF in the early universe — which, as we show, can be a leading order effect — is properly accounted for.

In this paper, we compute the cross-sections for the radiative capture into bound states of non-relativistic particles transforming under a non-Abelian gauge group. We consider, in particular, unbroken non-Abelian theories in the regime where the gauge coupling is perturbative. We do not specify the gauge group or the representation of the interacting particles, such that our results are applicable in a variety of models. Rather than an effective field theory approach [47] that has been employed in other studies [6, 8, 48–56], we use the method described in ref. [57], where the non-relativistic approximation is carried out directly on the relativistic amplitude.

We apply our results to a simplified model where DM is co-annihilating with scalar particles transforming in the fundamental of $\mathrm{SU}(3)_c$, and show that BSF has a very important effect on the DM relic density. In the MSSM incarnations of this scenario, the coloured particles typically possess also a sizeable coupling to the Higgs boson, which has been shown to mediate a sufficiently long-range interaction that enhances the annihilation cross-section [58]. While we do not consider it here, the attractive force mediated by the Higgs is expected to make the BSF effect more pronounced [59].

The formation of bound states in non-Abelian theories and their implications for DM have been considered in previous works. Reference [8] considered DM transforming under the adjoint of $\mathrm{SU}(2)_L$ (Wino-like DM), and performed computations in the broken electroweak phase, with the purpose of estimating the DM indirect detection signals. References [48–51] considered BSF via non-radiative scattering processes that can take

[1] Bound states may occur also in the spectrum of theories with contact interactions, in particular in the form of non-topological solitons [27–29], which have been considered in the context of DM [30, 31].

JHEP07(2018)096

place at a high rate in a thermal bath, and computed the effect of these processes on the DM density. Various rearrangement processes in Abelian and non-Abelian theories have been discussed in ref. [60]. Finally, refs. [55, 56] considered radiative BSF in unbroken non-Abelian theories. Our computations disagree with those of [55, 56] on the relative sign of the Abelian and non-Abelian diagrams contributing to these processes, but are in agreement with the dissociation rate of heavy quarkonium via gluon absorption computed in earlier work [61]. For the capture of a particle-antiparticle pair into its tightest bound state — which is typically the most significant capture process — our results imply that the leading order contributions add up, rather than partially canceling each other. This has very significant phenomenological implications, as we showcase in section 3.

The paper is organised as follows. In section 2, we compute the radiative BSF cross-sections. In section 3, we calculate the DM freeze-out including BSF in the scenario of DM co-annihilation with coloured partners. We conclude in section 4. Several important calculations are included in the appendices. In particular, in appendix B, we compute the overlap integrals that enter the BSF cross-sections. In appendix C, we adopt an effective field theory standpoint, we derive the non-relativistic Hamiltonian of the interactions that determine the formation of bound states, and point out the disagreement with previous works [55, 56]. This provides an independent check of the validity of our results.

2 Radiative bound-state formation in non-Abelian theories

We consider two complex scalar fields X_1 and X_2, transforming in the representations $\mathbf{R_1}$ and $\mathbf{R_2}$ of a non-Abelian gauge group $\mathbf{G}$. The Lagrangian is

$$\mathcal{L} = (D_\mu X_1)^\dagger (D^\mu X_1) + (D_\mu X_2)^\dagger (D^\mu X_2) - m_1^2 |X_1|^2 - m_2^2 |X_2|^2 , \tag{2.1}$$

where $D_\mu = \partial_\mu + i g_s G_\mu^a T^a$ is the covariant derivative, with G_μ^a being the gluon fields (we shall denote the corresponding particles with g, as usual) and $T^a = T_1^a$ or T_2^a being the generators of X_1 and X_2 respectively. The fine structure constant is

$$\alpha_s \equiv g_s^2/(4\pi) . \tag{2.2}$$

In the following, we shall compute the radiative BSF processes

$$X_1 + X_2 \to \mathcal{B}(X_1 X_2) + g . \tag{2.3}$$

While we express our results in terms of the capture processes (2.3), it is straightforward to generalise them to transitions between scattering states (bremsstrahlung) and bound-state excitation or de-excitation processes, by simply substituting the appropriate wavefunctions for the initial and final states [57]. Since we shall only compute the leading order terms to these transition processes, our results apply also to fermionic X_1 and/or X_2. Spin-orbit coupling arises only in higher orders in the non-relativistic regime.

We begin in section 2.1, with a summary of various formulae we use in our computations. In section 2.2, we give the interaction potential, and discuss the running of α_s. In section 2.3, we compute the amplitude for the transitions (2.3), for general representations

JHEP07(2018)096

and masses of X_1 and X_2. In section 2.4 we apply the result to particles in conjugate representations, but with arbitrary masses. For transitions involving a colour-singlet scattering or bound state, we compute explicitly the projected amplitude, and in section 2.5, we calculate the corresponding cross-sections.

2.1 Definitions and useful formulae

For easy reference, we first summarise various formualae that will be used in the following sections.

We define the total and the reduced mass of the interacting particles,

$$M \equiv m_1 + m_2\,, \qquad \mu \equiv \frac{m_1 m_2}{m_1 + m_2}\,, \tag{2.4}$$

and the dimensionless factors

$$\eta_1 \equiv \frac{m_1}{m_1 + m_2}\,, \qquad \eta_2 \equiv \frac{m_2}{m_1 + m_2}\,. \tag{2.5}$$

For the momenta p_1 and p_2 of X_1 and X_2, we shall often use the following momentum transformation, which allows to separate the center-of-momentum (CM) from the relative motion [57, 62],

$$P \equiv p_1 + p_2, \qquad p \equiv \eta_2 p_1 - \eta_1 p_2, \tag{2.6a}$$

$$p_1 = \eta_1 P + p, \qquad p_2 = \eta_2 P - p. \tag{2.6b}$$

Let $S_1(p_1)$ and $S_2(p_2)$ be the propagators of the X_1 and X_2,

$$S_j(p_j) \equiv \frac{i}{p_j^2 - m_j^2 + i\epsilon}\,, \qquad i = 1, 2\,. \tag{2.7}$$

For convenience, we also define

$$S(p; P) \equiv S_1(\eta_1 P + p)\; S_2(\eta_2 P - p)\,, \tag{2.8}$$

$$\mathcal{S}_0(\mathbf{p}; P) \equiv \int \frac{dp^0}{2\pi}\; S(p; P)\,. \tag{2.9}$$

To leading order in the non-relativistic regime [57, appendix C],

$$\mathcal{S}_0(\mathbf{p}; P) \simeq \left[-i4M\mu\left(P^0 - M - \frac{\mathbf{P}^2}{2M} - \frac{\mathbf{p}^2}{2\mu}\right)\right]^{-1}\,, \tag{2.10}$$

and [57, appendix E]

$$\int \frac{dq^0}{2\pi}\frac{dp^0}{2\pi}\; \frac{S(q; K)\, S_1(\eta_1 P + p)}{\mathcal{S}_0(\mathbf{q}; K)\, \mathcal{S}_0(\mathbf{p}; P)}\; (2\pi)^4\, \delta^4(q - p - \eta_2 P_g) \simeq 2m_2\; (2\pi)^3\, \delta^3(\mathbf{q} - \mathbf{p} - \eta_2 \mathbf{P}_g), \tag{2.11a}$$

$$\int \frac{dq^0}{2\pi}\frac{dp^0}{2\pi}\; \frac{S(q; K)\, S_2(\eta_1 P - p)}{\mathcal{S}_0(\mathbf{q}; K)\, \mathcal{S}_0(\mathbf{p}; P)}\; (2\pi)^4\, \delta^4(q - p + \eta_1 P_g) \simeq 2m_1\; (2\pi)^3\, \delta^3(\mathbf{q} - \mathbf{p} + \eta_1 \mathbf{P}_g). \tag{2.11b}$$

As we shall see in section 2.3, we use eqs. (2.10) and (2.11) to integrate out the virtuality of X_1, X_2 in the radiative part of the BSF diagrams.

JHEP07(2018)096

2.2 Potential and the running of the coupling

The interaction between X_1 and X_2 can be decomposed into irreducible representations,

$$\mathbf{R_1} \otimes \mathbf{R_2} = \sum_{\hat{\mathbf{R}}} \hat{\mathbf{R}} \,. \tag{2.12}$$

For each $\hat{\mathbf{R}}$, the interaction is described in the non-relativistic regime by a static Coulomb potential [63]

$$V(r) = -\alpha_g / r \,, \tag{2.13}$$

where the coupling α_g is related to α_s according to

$$\alpha_g = \alpha_s \times \frac{1}{2}[C_2(\mathbf{R_1}) + C_2(\mathbf{R_2}) - C_2(\hat{\mathbf{R}})] \,. \tag{2.14}$$

Here, $C_2(\mathbf{R})$ is the quadratic Casimir invariant of the representation $\mathbf{R}$. The Coulomb potential (2.13) distorts the scattering-state wavefunctions and, if attractive, gives rise to bound states. The scattering-state and bound-state wavefunctions are reviewed in appendix A.

In general, the coupling α_s depends on the momentum transfer Q,

$$\alpha_s = \alpha_s(Q) \,, \tag{2.15}$$

which is different in the various interaction vertices that appear in the transitions we consider. In table 1, we list the various vertices, specify the symbols we use, and give the average Q in each case.

2.3 Amplitude for radiative transitions

Radiative transitions are represented by the diagram of figure 1a, which can be separated into the wavefunctions of the asymptotic states and the radiative vertex. The wavefunctions resum the two-particle interactions at infinity. The long-range $X_1 - X_2$ interaction arises from the one-gluon exchange kernel, which gives rise to the static potential of eq. (2.13) in the non-relativistic regime. The low momentum transfer ($\sim \mu v_{\rm rel}$ for the scattering states and $\sim \mu\alpha_s$ for the bound states) via the exchanged gluons is responsible for the appearance of non-perturbative phenomena, the Sommerfeld effect [64, 65] and the mere existence of bound states. The radiative vertex is computed perturbatively, with the leading order contributions shown in figure 1b. We discuss them further below.

In the instantaneous approximation, the amplitude for the radiative capture into a bound state is [57]

$$[\mathcal{M}^{\nu}_{\mathbf{k}\to\{n\ell m\}}]^{a}_{ii',jj'} = \frac{1}{\sqrt{2\mu}} \int \frac{d^3q}{(2\pi)^3} \frac{d^3p}{(2\pi)^3} \; \tilde{\psi}^{*}_{n\ell m}(\mathbf{p}) \; \tilde{\phi}_{\mathbf{k}}(\mathbf{q}) \; [\mathcal{M}^{\nu}_{\rm trans}(\mathbf{q},\mathbf{p})]^{a}_{ii',jj'} \,, \tag{2.16}$$

where the Latin indices i, i', j, j' and a denote the colour of the initial and final state particles, as shown in figure 1b, and $\tilde{\phi}_{\mathbf{k}}(\mathbf{q})$ and $\tilde{\psi}_{n\ell m}(\mathbf{p})$ are the scattering-state and bound-state wavefunctions in momentum space that obey the Schrödinger equation. Here, $\mathbf{q}$

JHEP07(2018)096

Vertices	$\boldsymbol{\alpha_s}$	$\boldsymbol{\alpha_g}$	**Average momentum transfer $\boldsymbol{Q}$**
Wavefunction (ladder diagrams) of scattering state in colour rep. $\hat{\mathbf{R}}$	α_s^S	$\alpha^S_{g,[\hat{\mathbf{R}}]} = (\alpha_s^S/2)\times$ $\times\,[C_2(\mathbf{R_1}) + C_2(\mathbf{R_2}) - C_2(\hat{\mathbf{R}})]$	$k \equiv \mu\, v_{\rm rel}$
Wavefunction (ladder diagrams) of bound state in colour rep. $\hat{\mathbf{R}}$	$\alpha^B_{s,[\hat{\mathbf{R}}]}$	$\alpha^B_{g,[\hat{\mathbf{R}}]} = (\alpha^B_{s,[\hat{\mathbf{R}}]}/2)\times$ $\times\,[C_2(\mathbf{R_1}) + C_2(\mathbf{R_2}) - C_2(\hat{\mathbf{R}})]$	$\kappa_{\hat{\mathbf{R}}} \equiv \mu\, \alpha^B_{g,[\hat{\mathbf{R}}]}$
Formation of bound states of colour rep. $\hat{\mathbf{R}}$: gluon emission	$\alpha^{\rm BSF}_{s,[\hat{\mathbf{R}}]}$		$\mathcal{E}_{\mathbf{k}} - \mathcal{E}_{n\ell} =$ $\frac{\mu}{2}\left[v^2_{\rm rel} + (\alpha^B_{g,[\hat{\mathbf{R}}]}/n)^2\right]$
$gX_i^\dagger X_i$ vertices in non-Abelian diagram for capture in colour rep. $\hat{\mathbf{R}}$	$\alpha^{\rm NA}_{s,[\hat{\mathbf{R}}]}$		$\mu\sqrt{v^2_{\rm rel} + {\alpha^B_{g,[\hat{\mathbf{R}}]}}^2}$

Table 1. The momentum transfer Q at which the coupling $\alpha_s(Q)$ is evaluated. With the exception of α_s^S, the couplings depend on the representation $\hat{\mathbf{R}}$, as denoted; however, in our general computations, we shall often omit the representation index, for brevity.

$(-\mathbf{q})$ and $\mathbf{p}$ $(-\mathbf{p})$ are the 3-momenta of $X_1(X_2)$ in the CM frame, in the scattering state and in the bound state, respectively. The scattering state wavefunction is characterised by the continuous quantum number $\mathbf{k}$, which specifies the expectation value of $\mathbf{q}$. In a central potential, such as eq. (2.13), the bound state wavefunction is characterised by the standard discrete principal and angular-momentum quantum numbers $\{n, \ell, m\}$, which specify the expectation value of $\mathbf{p}$. The wavefunctions in a Coulomb potential are reviewed in appendix A.[2]

$\mathcal{M}^\nu_{\rm trans}(\mathbf{q}, \mathbf{p})$ is the perturbative transition amplitude with the virtuality of the interacting particles integrated out, as follows [57, section 3.3]

$$[\mathcal{M}^\nu_{\rm trans}(\mathbf{q}, \mathbf{p})]^a_{ii',jj'} = \frac{1}{\mathcal{S}_0(\mathbf{q}; K)\,\mathcal{S}_0(\mathbf{p}; P)} \int \frac{dq^0}{2\pi}\frac{dp^0}{2\pi}\, [\mathcal{C}^\nu(q, p; K, P)]^a_{ii',jj'}\,. \tag{2.17}$$

Here, $[\mathcal{C}^\nu(q, p; K, P)]^a_{ii',jj'}$ is the sum of all connected diagrams contributing to the process

$$X_{1,i}\,(\eta_1 K + q) + X_{2,j}\,(\eta_2 K - q) \to X_{1,i'}\,(\eta_1 P + p) + X_{2,j'}\,(\eta_2 P - p) + g^a(P_g), \tag{2.18}$$

[2] We note that the integrand in eq. (2.16) admits corrections of higher order in $\mathbf{q}$ and $\mathbf{p}$ that arise from the relativistic normalisation of states. Here we are interested only in the leading order terms, and we shall neglect these corrections. However, these corrections become important when there is a cancellation between the lowest order contributions to $\mathcal{M}_{\rm trans}$ [9, 57].

JHEP07(2018)096

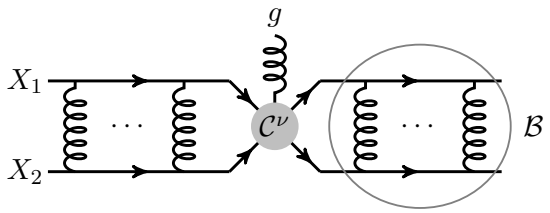

(a) The amplitude for the radiative capture consists of the (non-perturbative) initial and final state wavefunctions, and the perturbative 5-point function that includes the radiative vertices.

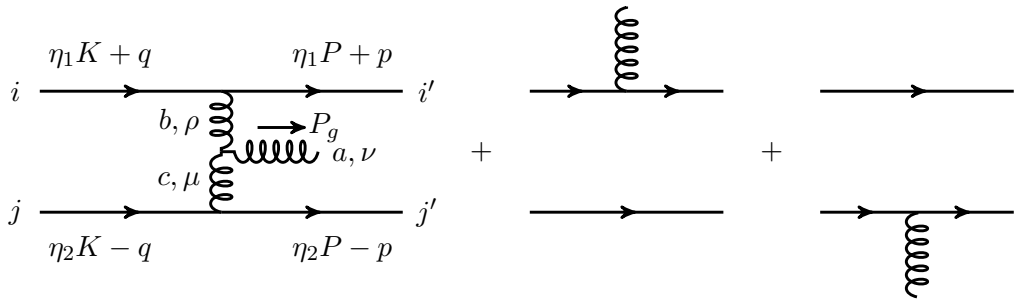

(b) The leading order diagrams contributing to $\mathcal{C}^\nu$. The external-momentum, colour-index and space-time-index assignments are the same in all three diagrams.

Figure 1. Radiative capture into bound states.

with the incoming and outgoing X_1, X_2 being off-shell and only the emitted gluon g being on-shell and amputated. We emphasise that the X_1, X_2 incoming and outgoing legs should *not* be amputated in the computation of $\mathcal{C}^\nu$; the proper amputation is done by the prefactor in eq. (2.17). (We recall that $\mathcal{S}_0$ is defined in eq. (2.9).) Note that the connected diagrams contributing to $\mathcal{C}^\nu$ may include not-fully-connected diagrams that are non-zero due to the off-shellness of the legs, such as the diagrams in which the radiation is emitted from one of the legs (cf. figure 1b).[3]

In eq. (2.18), the momenta of the particles are indicated inside the parentheses. While the 3-momenta $\mathbf{q}$ and $\mathbf{p}$ follow the probability distributions given by the wavefunctions $\tilde{\phi}_{\mathbf{k}}(\mathbf{q})$ and $\tilde{\psi}_{n\ell m}(\mathbf{p})$ that appear in eq. (2.16), q^0 and p^0 are determined by the poles of $\mathcal{C}^\nu$, upon the integration denoted in eq. (2.17). The total 4-momenta of the scattering state, the bound state and the radiated gluon, K, P and P_g respectively, essentially contain all the (discrete and continuous) quantum numbers that fully specify the system. In the non-relativistic regime, they can be expressed as

$$K = \left(M + \frac{\mathbf{K}^2}{2M} + \mathcal{E}_{\mathbf{k}},\ \mathbf{K} \right) , \tag{2.19a}$$

$$P = \left(M + \frac{\mathbf{P}^2}{2M} + \mathcal{E}_{n\ell},\ \mathbf{P} \right) , \tag{2.19b}$$

$$P_g = (\omega,\ \mathbf{P}_g) , \tag{2.19c}$$

[3] If in a certain theory, all diagrams contributing to (2.18) are fully connected, then $\mathcal{M}_{\text{trans}}$ can be computed at leading order from the sum of the fully amputated diagrams by simply setting all incoming and outgoing particles on-shell [57].

JHEP07(2018)096

where $\mathcal{E}_{\mathbf{k}} = \mathbf{k}^2/(2\mu) = \mu v_{\rm rel}^2/2$ is the kinetic energy of the scattering state in the CM frame, with $v_{\rm rel}$ being the relative velocity of the interacting particles, and $\mathcal{E}_{n\ell} < 0$ is the binding energy of the bound state. Note that $M_{n\ell} \equiv M + \mathcal{E}_{n\ell}$ is the mass of the bound state. For a Coulomb potential, $\mathcal{E}_{n\ell} = -\kappa^2/(2n^2\mu)$, with $\kappa \equiv \mu\alpha_s^B$ (cf. appendix A). Energy-momentum conservation, $K = P + P_g$, implies

$$\omega = |\mathbf{P}_g| \simeq \mathcal{E}_{\mathbf{k}} - \mathcal{E}_{n\ell}\,. \tag{2.20}$$

The leading order contributions to $[\mathcal{C}^\nu]^a_{ii',jj'}$ are shown in figure 1b. We compute them next using the Feynman rules from [66].

Emission from the mediator.

$$\begin{aligned}
&i(\mathcal{C}^\nu_{\rm med})^a_{ii',jj'} = \\
&= S_1(\eta_1 P + p)\left[-ig_s(T_1^b)_{i'i}\ (\eta_1 K + \eta_1 P + q + p)_\rho\right] S_1(\eta_1 K + q)\ \frac{-i}{(\eta_1 K + q - \eta_1 P - p)^2} \\
&\quad \times S_2(\eta_2 P - p)\left[-ig_s\,(T_2^c)_{j'j}\ (\eta_2 K + \eta_2 P - q - p)_\mu\right] S_2(\eta_2 K - q)\ \frac{-i}{(\eta_2 K - q - \eta_2 P + p)^2} \\
&\quad \times (-g_s^{\rm BSF} f^{abc})\ \{g^{\rho\mu}[(\eta_1 K + q - \eta_1 P - p) - (\eta_2 K - q - \eta_2 P + p)]^\nu \\
&\quad + g^{\nu\rho}[-P_g - (\eta_1 K + q - \eta_1 P - p)]^\mu + g^{\mu\nu}[(\eta_2 K - q - \eta_2 P + p) + P_g]^\rho\}\,,
\end{aligned} \tag{2.21a}$$

Emission from X_1.

$$\begin{aligned}
i(\mathcal{C}_1^\nu)^a_{ii',jj'} = \delta_{j'j}\ S_2(\eta_2 K - q) \times S_1(\eta_1 P + p)\, S_1(\eta_1 K + q) \\
\times \left[-ig_s^{\rm BSF}(T_1^a)_{i'i}\ (\eta_1 K + \eta_1 P + q + p)^\nu\,(2\pi)^4\delta^4(\eta_1 K + q - \eta_1 P - p - P_g)\right],
\end{aligned} \tag{2.21b}$$

Emission from X_2.

$$\begin{aligned}
i(\mathcal{C}_2^\nu)^a_{ii',jj'} = \delta_{i'i}\ S_1(\eta_1 K + q) \times S_2(\eta_2 P - p)\, S_2(\eta_2 K - q) \\
\times \left[-ig_s^{\rm BSF}\,(T_2^a)_{j'j}\ (\eta_2 K + \eta_2 P - q - p)^\nu\,(2\pi)^4\delta^4(\eta_2 K - q - \eta_2 P + p - P_g)\right].
\end{aligned} \tag{2.21c}$$

We are interested only in the spatial components of $\mathcal{C}^\nu$, $\nu = 1, 2, 3$,

$$\boldsymbol{\mathcal{C}}^a_{ii',jj'} = (\boldsymbol{\mathcal{C}}_{\rm med})^a_{ii',jj'} + (\boldsymbol{\mathcal{C}}_1)^a_{ii',jj'} + (\boldsymbol{\mathcal{C}}_2)^a_{ii',jj'}\,. \tag{2.22}$$

The wavefunctions in eq. (2.16) impose $|\mathbf{q}| \sim k = \mu v_{\rm rel}$ and for a Coulomb potential $|\mathbf{p}| \sim \kappa/n = \mu\alpha_s^B/n$. Noting the hierarchy of scales $|\mathbf{q}|, |\mathbf{p}|, k, \kappa \ll M, \mu$, and using eqs. (2.19) and (2.20), we find from eqs. (2.21) that to leading order in $v_{\rm rel}$ and α_s, in the CM frame,

$$(\boldsymbol{\mathcal{C}}_{\rm med})^a_{ii',jj'} \simeq +if^{abc}\,(T_1^b)_{i'i}(T_2^c)_{j'j} \times 8g_s^{\rm BSF} g_s^2\, M\mu\ \frac{(\mathbf{q}-\mathbf{p})}{(\mathbf{q}-\mathbf{p})^4} \times S(q;K)\,S(p;P), \tag{2.23a}$$

$$(\boldsymbol{\mathcal{C}}_1)^a_{ii',jj'} \simeq -\,(T_1^a)_{i'i}\,\delta_{j'j} \times g_s^{\rm BSF}\ (\mathbf{q}+\mathbf{p}) \times S(q;K)\,S_1(\eta_1 P + p)\ (2\pi)^4\delta^4(q - p - \eta_2 P_g), \tag{2.23b}$$

$$(\boldsymbol{\mathcal{C}}_2)^a_{ii',jj'} \simeq +\delta_{i'i}\,(T_2^a)_{j'j} \times g_s^{\rm BSF}\ (\mathbf{q}+\mathbf{p}) \times S(q;K)\,S_2(\eta_2 P - p)\ (2\pi)^4\delta^4(q - p + \eta_1 P_g). \tag{2.23c}$$

A few comments on $\boldsymbol{\mathcal{C}}_{\rm med}$ are in order.

JHEP07(2018)096

- The leading order contribution arises from the contraction of the momenta of the two vertices on the scalar legs.

- The factor g_s^2 arises from the same vertices, where the momentum transfer is $\sim |\mathbf{p}-\mathbf{q}|$, with $|\mathbf{p}| \sim \kappa = \mu\alpha_g^B$ and $|\mathbf{q}| \sim k = \mu v_{\rm rel}$. This implies that g_s should be evaluated at the scale $Q \approx \sqrt{\kappa^2+k^2}$ (cf. table 1).[4]

- In eq. (2.23a), we have neglected the energy transfer along the gluon propagators (as is also done in the one-boson exchange diagrams that are resummed into the non-relativistic potential). Upon the integration indicated in eq. (2.17), the poles of the scalar propagators, $S(q;K)\,S(p;P)$, set $q^0 \sim \mathbf{q}^2/\mu \sim \mathbf{k}^2/\mu$ and $p^0 \sim \mathbf{p}^2/\mu \sim \kappa^2/\mu$. In contrast, the poles of the gluon propagators set $q^0 - p^0 \sim |\mathbf{q}-\mathbf{p}| \sim \sqrt{\mathbf{k}^2+\kappa^2}$. Since q^0 and p^0 indicate the off-shellness of the two scalar particles, the gluon poles — on which the off-shellness of the scalars is greater for $\alpha_s, v_{\rm rel} < 1$ — yield subdominant contributions to the transition amplitude.

- Naively, $\boldsymbol{\mathcal{C}}_{\rm med}$ may be expected to be of higher order in α_s than $\boldsymbol{\mathcal{C}}_1$ and $\boldsymbol{\mathcal{C}}_2$. However, the scaling of $q^0, p^0, |\mathbf{q}|$ and $|\mathbf{p}|$ with α_s and $v_{\rm rel}$ described above implies all three diagrams are of the same order. This will become apparent in the following.

Collecting eqs. (2.17), (2.22) and (2.23), and using eqs. (2.9) and (2.11), we find

$$\begin{aligned}[\boldsymbol{\mathcal{M}}_{\rm trans}]^a_{ii',jj'} \simeq -g_s^{\rm BSF} 4M \Big\{ & -if^{abc}(T_1^b)_{i'i}(T_2^c)_{j'j} \times 8\pi\mu\alpha_s^{\rm NA}\,\frac{\mathbf{q}-\mathbf{p}}{(\mathbf{q}-\mathbf{p})^4} \\ & + \eta_2\,(T_1^a)_{i'i}\,\delta_{j'j} \times \mathbf{p}\,(2\pi)^3\,\delta^3(\mathbf{q}-\mathbf{p}-\eta_2\mathbf{P}_g) \\ & -\eta_1\,\delta_{i'i}\,(T_2^a)_{j'j} \times \mathbf{p}\,(2\pi)^3\,\delta^3(\mathbf{q}-\mathbf{p}+\eta_1\mathbf{P}_g)\Big\}\,. \end{aligned} \tag{2.24}$$

Plugging eq. (2.24) into eq. (2.16), we obtain

$$\begin{aligned}[\boldsymbol{\mathcal{M}}_{\mathbf{k}\to\{n\ell m\}}]^a_{ii',jj'} = -\left(2^5\pi\alpha_s^{\rm BSF}\,M^2/\mu\right)^{1/2} \times \Big\{ & -if^{abc}(T_1^b)_{i'i}(T_2^c)_{j'j}\;\boldsymbol{\mathcal{Y}}_{\mathbf{k},\{n\ell m\}} \\ & + \eta_2\,(T_1^a)_{i'i}\,\delta_{j'j}\;\boldsymbol{\mathcal{J}}_{\mathbf{k},\{n\ell m\}}(\eta_2\mathbf{P}_g) - \eta_1\,\delta_{i'i}\,(T_2^a)_{j'j}\;\boldsymbol{\mathcal{J}}_{\mathbf{k},\{n\ell m\}}(-\eta_1\mathbf{P}_g)\Big\}\,, \end{aligned} \tag{2.25}$$

where we have defined the overlap vector integrals (see also [9, 57])

$$\boldsymbol{\mathcal{J}}_{\mathbf{k},\{n\ell m\}}(\mathbf{b}) \equiv \int \frac{d^3p}{(2\pi)^3}\;\mathbf{p}\,\tilde{\psi}^*_{n\ell m}(\mathbf{p})\,\tilde{\phi}_{\mathbf{k}}(\mathbf{p}+\mathbf{b})\,, \tag{2.26a}$$

$$\boldsymbol{\mathcal{Y}}_{\mathbf{k},\{n\ell m\}} \equiv 8\pi\mu\alpha_s^{\rm NA} \int \frac{d^3p}{(2\pi)^3}\frac{d^3q}{(2\pi)^3}\;\frac{\mathbf{q}-\mathbf{p}}{(\mathbf{q}-\mathbf{p})^4}\,\tilde{\psi}^*_{n\ell m}(\mathbf{p})\,\tilde{\phi}_{\mathbf{k}}(\mathbf{q})\,. \tag{2.26b}$$

$\boldsymbol{\mathcal{J}}_{\mathbf{k},\{n\ell m\}}$ has been computed in refs. [9, 57]. We review the result, and compute $\boldsymbol{\mathcal{Y}}_{\mathbf{k},\{n\ell m\}}$ in appendix B.

[4] Since BSF is insignificant when $\kappa \ll k$, in section 3 we approximate the momentum transfer in these vertices with that inside the bound state, $Q \sim \kappa$, thus setting $\alpha_s^{\rm NA} = \alpha_s^B$.

JHEP07(2018)096

2.4 Colour decomposition for conjugate representations

We now focus on particles transforming under conjugate representations $\mathbf{R}_1 = \mathbf{R}$ and $\mathbf{R}_2 = \bar{\mathbf{R}}$, such that

$$T_1^a = T^a\,, \qquad T_2^a = -T^{a\,*}\,. \tag{2.27}$$

We shall *not* assume though that the masses of the interacting particles are equal, so that our results are more widely applicable. For the overlap integral $\boldsymbol{\mathcal{J}}_{\mathbf{k}\to\{n\ell m\}}(\mathbf{b})$, with $|\mathbf{b}| \propto |\mathbf{P}_g|$, the dominant contribution is independent of $\mathbf{b}$ [9, 57]. In the following, we denote $\boldsymbol{\mathcal{J}}_{\mathbf{k},\{n\ell m\}} = \boldsymbol{\mathcal{J}}_{\mathbf{k},\{n\ell m\}}(\mathbf{b}=0)$, and the amplitude (2.25) becomes

$$\begin{aligned}[\boldsymbol{\mathcal{M}}_{\mathbf{k}\to\{n\ell m\}}]^a_{ii',jj'} = &-(2^5\pi\alpha_s^{\text{BSF}}\,M^2/\mu)^{1/2}\times\\ &\times\Big\{\left(\eta_2\,T^a_{i'i}\,\delta_{j'j}+\eta_1\,\delta_{i'i}\,T^a_{jj'}\right)\,\boldsymbol{\mathcal{J}}_{\mathbf{k},\{n\ell m\}}+if^{abc}T^b_{i'i}T^c_{jj'}\boldsymbol{\mathcal{Y}}_{\mathbf{k},\{n\ell m\}}\Big\}\,.\end{aligned} \tag{2.28}$$

The tensor product of two conjugate representations contains always a singlet and an adjoint, and possibly other states,

$$\mathbf{R}\otimes\bar{\mathbf{R}} = \mathbf{1}\oplus\mathbf{adj}\oplus\cdots\,. \tag{2.29}$$

It is clear from eq. (2.14) that, among all irreducible representations, the singlet configuration ($C_2(\mathbf{1}) = 0$) exhibits the most attractive potential, and thus accommodates the tightest bound state. Equation (2.29) implies that at least the following capture processes are allowed by the group algebra, provided that the potential in the final state is attractive, such that the bound state exists:

$$(X+X^\dagger)_{[\mathbf{adj}]} \to \mathcal{B}(XX^\dagger)_{[\mathbf{1}]} + g_{[\mathbf{adj}]}\,, \tag{2.30a}$$

$$(X+X^\dagger)_{[\mathbf{1}]} \to \mathcal{B}(XX^\dagger)_{[\mathbf{adj}]} + g_{[\mathbf{adj}]}\,, \tag{2.30b}$$

$$(X+X^\dagger)_{[\mathbf{adj}]} \to \mathcal{B}(XX^\dagger)_{[\mathbf{adj}]} + g_{[\mathbf{adj}]}\,. \tag{2.30c}$$

Depending on the group $\mathbf{G}$ and the representation $\mathbf{R}$, more transitions may be possible. The amplitudes for the various transitions may be computed from eq. (2.28) by projecting onto the appropriate colour representations, using the Clebsch-Gordan coefficients. Below we compute explicitly the amplitudes for the transitions (2.30a) and (2.30b) only.

In the following, $d_{\mathbf{R}}$, $C(\mathbf{R})$ and $C_2(\mathbf{R})$ stand for the dimension and the Casimir invariants of the representation $\mathbf{R}$, and $d_{\mathbf{G}}$, $C(\mathbf{G})$ and $C_2(\mathbf{G})$ are the corresponding quantities for the group $\mathbf{G}$. Evidently, the wavefunctions and therefore $\boldsymbol{\mathcal{J}}_{\mathbf{k},\{n\ell m\}}$ and $\boldsymbol{\mathcal{Y}}_{\mathbf{k},\{n\ell m\}}$ depend on the colour representations of the scattering and bound states, $\mathbf{R}_S$ and $\mathbf{R}_B$. Whenever appropriate, we shall use the notation $\boldsymbol{\mathcal{J}}^{[\mathbf{R}_S,\mathbf{R}_B]}_{\mathbf{k},\{n\ell m\}}$ and $\boldsymbol{\mathcal{Y}}^{[\mathbf{R}_S,\mathbf{R}_B]}_{\mathbf{k},\{n\ell m\}}$.

2.4.1 Adjoint scattering states to singlet bound states

The radiative capture into colour-singlet bound states can occur *only* from adjoint scattering states,

$$(X+X^\dagger)_{[\mathbf{adj}]} \to \mathcal{B}(XX^\dagger)_{[\mathbf{1}]} + g_{[\mathbf{adj}]}\,. \tag{2.31}$$

JHEP07(2018)096

It thus suffices to project only the final $X - X^\dagger$ state onto the singlet configuration; upon summing the squared amplitude over colours, the group algebra will project the initial state onto the adjoint. The amplitude for the process (2.31) is

$$\begin{aligned}\left(\boldsymbol{\mathcal{M}}^{[\mathbf{adj}]\to[\mathbf{1}]}_{\mathbf{k}\to\{n\ell m\}}\right)^a_{i,j} &= \frac{\delta_{i'j'}}{\sqrt{d_{\mathbf{R}}}}\left(\boldsymbol{\mathcal{M}}_{\mathbf{k}\to\{n\ell m\}}\right)^a_{ii',jj'} \\ &= -\left(\frac{2^5\pi\alpha_s^{\mathrm{BSF}}\,M^2}{\mu}\right)^{1/2}\times\frac{1}{\sqrt{d_{\mathbf{R}}}}\left[T^a_{ji}\;\boldsymbol{\mathcal{J}}^{[\mathbf{adj},\mathbf{1}]}_{\mathbf{k},\{n\ell m\}}+if^{abc}(T^cT^b)_{ji}\;\boldsymbol{\mathcal{Y}}^{[\mathbf{adj},\mathbf{1}]}_{\mathbf{k},\{n\ell m\}}\right] \\ &= -\left(\frac{2^5\pi\alpha_s^{\mathrm{BSF}}\,M^2}{\mu}\right)^{1/2}\times\frac{1}{\sqrt{d_{\mathbf{R}}}}\left[\boldsymbol{\mathcal{J}}^{[\mathbf{adj},\mathbf{1}]}_{\mathbf{k},\{n\ell m\}}+\frac{C_2(\mathbf{G})}{2}\;\boldsymbol{\mathcal{Y}}^{[\mathbf{adj},\mathbf{1}]}_{\mathbf{k},\{n\ell m\}}\right]T^a_{ji}\,, \end{aligned}\tag{2.32}$$

where in the last step we used $f^{abc}T^bT^c = (i/2)\,C_2(\mathbf{G})\,T^a$. The amplitude squared, colour-summed and averaged over the colour of the initial particles is

$$\frac{1}{d_{\mathbf{R}}^2}\left|\boldsymbol{\mathcal{M}}^{[\mathbf{adj}]\to[\mathbf{1}]}_{\mathbf{k}\to\{n\ell m\}}\right|^2 = \left(\frac{2^5\pi\alpha_s^{\mathrm{BSF}}\,M^2}{\mu}\right)\times\frac{C_2(\mathbf{R})}{d_{\mathbf{R}}^2}\left|\boldsymbol{\mathcal{J}}^{[\mathbf{adj},\mathbf{1}]}_{\mathbf{k},\{n\ell m\}}+\frac{C_2(\mathbf{G})}{2}\;\boldsymbol{\mathcal{Y}}^{[\mathbf{adj},\mathbf{1}]}_{\mathbf{k},\{n\ell m\}}\right|^2. \tag{2.33}$$

2.4.2 Singlet scattering states to adjoint bound states

With the emission of a gluon, a colour-singlet scattering state can turn *only* into an adjoint state,

$$(X+X^\dagger)_{[\mathbf{1}]}\to\mathcal{B}(XX^\dagger)_{[\mathbf{adj}]}+g_{[\mathbf{adj}]}\,. \tag{2.34}$$

Similarly to the above, the amplitude for the process (2.34) is deduced from eq. (2.28) by projecting the initial $X - X^\dagger$ state onto the singlet configuration

$$\begin{aligned}\left(\boldsymbol{\mathcal{M}}^{[\mathbf{1}]\to[\mathbf{adj}]}_{\mathbf{k}\to\{n\ell m\}}\right)^a_{i',j'} &= \frac{\delta_{ij}}{\sqrt{d_{\mathbf{R}}}}\left(\boldsymbol{\mathcal{M}}_{\mathbf{k}\to\{n\ell m\}}\right)^a_{ii',jj'} \\ &= -\left(\frac{2^5\pi\alpha_s^{\mathrm{BSF}}\,M^2}{\mu}\right)^{1/2}\times\frac{1}{\sqrt{d_{\mathbf{R}}}}\left[T^a_{i'j'}\;\boldsymbol{\mathcal{J}}^{[\mathbf{1},\mathbf{adj}]}_{\mathbf{k},\{n\ell m\}}+if^{abc}(T^bT^c)_{i'j'}\boldsymbol{\mathcal{Y}}^{[\mathbf{1},\mathbf{adj}]}_{\mathbf{k},\{n\ell m\}}\right] \\ &= -\left(\frac{2^5\pi\alpha_s^{\mathrm{BSF}}\,M^2}{\mu}\right)^{1/2}\times\frac{1}{\sqrt{d_{\mathbf{R}}}}\left[\boldsymbol{\mathcal{J}}^{[\mathbf{1},\mathbf{adj}]}_{\mathbf{k},\{n\ell m\}}-\frac{C_2(\mathbf{G})}{2}\boldsymbol{\mathcal{Y}}^{[\mathbf{1},\mathbf{adj}]}_{\mathbf{k},\{n\ell m\}}\right]T^a_{i'j'}\,. \end{aligned}\tag{2.35}$$

Then,

$$\frac{1}{d_{\mathbf{R}}^2}\left|\boldsymbol{\mathcal{M}}^{[\mathbf{1}]\to[\mathbf{adj}]}_{\mathbf{k}\to\{n\ell m\}}\right|^2 = \left(\frac{2^5\pi\alpha_s^{\mathrm{BSF}}\,M^2}{\mu}\right)\times\frac{C_2(\mathbf{R})}{d_{\mathbf{R}}^2}\left|\boldsymbol{\mathcal{J}}^{[\mathbf{1},\mathbf{adj}]}_{\mathbf{k},\{n\ell m\}}-\frac{C_2(\mathbf{G})}{2}\;\boldsymbol{\mathcal{Y}}^{[\mathbf{1},\mathbf{adj}]}_{\mathbf{k},\{n\ell m\}}\right|^2. \tag{2.36}$$

2.4.3 Remaining transitions

Depending on $\mathbf{R}$, other transitions may be possible. In this case, appropriate projections of the amplitude (2.28) have to be computed. It is sometimes possible to obtain the amplitude-squared for a transition of interest from the total amplitude-squared by subtracting the contributions of other known transitions. For this reason, we provide here the total colour-averaged squared amplitude,

$$\begin{aligned}\frac{1}{d_{\mathbf{R}}^2}\left|\boldsymbol{\mathcal{M}}^{\mathbf{total}}_{\mathbf{k}\to\{n\ell m\}}\right|^2 &= \left(\frac{2^5\pi\alpha_s^{\mathrm{BSF}}\,M^2}{\mu}\right)\times \\ &\quad\times C_2(\mathbf{R})\left\{(\eta_1^2+\eta_2^2)\left|\boldsymbol{\mathcal{J}}_{\mathbf{k},\{n\ell m\}}\right|^2+\frac{C_2(\mathbf{R})C_2(\mathbf{G})}{d_{\mathbf{G}}}\left|\boldsymbol{\mathcal{Y}}_{\mathbf{k},\{n\ell m\}}\right|^2\right\}. \end{aligned}\tag{2.37}$$

JHEP07(2018)096

Note that $\boldsymbol{\mathcal{J}}_{\mathbf{k},\{n\ell m\}}$ and $\boldsymbol{\mathcal{Y}}_{\mathbf{k},\{n\ell m\}}$ depend on the representations of the scattering and the bound states. Thus, if more than one transitions are possible, in which either the scattering and/or the bound states belong to different representations, then their contributions to eq. (2.37) need to be separated, and $\boldsymbol{\mathcal{J}}_{\mathbf{k},\{n\ell m\}}$, $\boldsymbol{\mathcal{Y}}_{\mathbf{k},\{n\ell m\}}$ should be evaluated using the wavefunctions of the corresponding representations.

2.5 Cross-sections for capture into the ground state

The differential BSF cross-section for capture into the ground state $\{n\ell m\} = \{100\}$ is given by

$$v_{\rm rel}\frac{d\sigma_{\mathbf{k}\to\{100\}}}{d\Omega} = \frac{|\mathbf{P}_g|}{64\pi^2 M^2\mu}\left(|\boldsymbol{\mathcal{M}}_{\mathbf{k}\to\{100\}}|^2 - |\hat{\mathbf{P}}_g\cdot\boldsymbol{\mathcal{M}}_{\mathbf{k}\to\{100\}}|^2\right), \tag{2.38}$$

where energy-momentum conservation implies (cf. eq. (2.20))

$$|\mathbf{P}_g| = \mathcal{E}_{\mathbf{k}} - \mathcal{E}_{10} = \frac{\mu}{2}\left[\left(\alpha_g^B\right)^2 + v_{\rm rel}^2\right]. \tag{2.39}$$

The leading-order contributions to the amplitude are $\boldsymbol{\mathcal{J}}_{\mathbf{k},\{100\}} \propto \hat{\mathbf{k}}$ and $\boldsymbol{\mathcal{Y}}_{\mathbf{k},\{100\}} \propto \hat{\mathbf{k}}$ (cf. refs. [9, 57] and appendix B). Thus

$$|\boldsymbol{\mathcal{M}}_{\mathbf{k}\to\{100\}}|^2 - |\hat{\mathbf{P}}_g\cdot\boldsymbol{\mathcal{M}}_{\mathbf{k}\to\{100\}}|^2 = |\boldsymbol{\mathcal{M}}_{\mathbf{k}\to\{100\}}|^2\sin^2\theta\,,$$

where θ is the angle between $\mathbf{k}$ and $\mathbf{P}_g$, and $|\boldsymbol{\mathcal{M}}_{\mathbf{k}\to\{100\}}|^2$ is independent of θ. Thus,

$$\sigma_{\mathbf{k}\to\{100\}}v_{\rm rel} = \frac{(\alpha_g^B)^2 + v_{\rm rel}^2}{48\pi M^2}\,|\boldsymbol{\mathcal{M}}_{\mathbf{k}\to\{100\}}|^2\,. \tag{2.40}$$

For convenience, in the following we shall use the parameters [cf. eqs. (A.6)]

$$\zeta_S \equiv \alpha_g^S/v_{\rm rel}\,, \tag{2.41a}$$
$$\zeta_B \equiv \alpha_g^B/v_{\rm rel}\,. \tag{2.41b}$$

From the amplitudes of eqs. (2.33), (2.36) and (2.37), and the expressions (B.4) for the overlap integrals $\boldsymbol{\mathcal{J}}$ and $\boldsymbol{\mathcal{Y}}$, we find that the colour-averaged BSF cross-sections are

$$\sigma_{\mathbf{k}\to\{100\}}v_{\rm rel} = \frac{\pi\alpha_s^{\rm BSF}\alpha_g^B}{\mu^2}\,\frac{2^7 C_2(\mathbf{R})}{3d_{\mathbf{R}}^2}\,f_c\times S_{\rm BSF}(\zeta_S,\zeta_B)\,, \tag{2.42a}$$

where f_c is a numerical factor that depends on the transition,

$$f_c = \begin{cases} \left[1 + \dfrac{C_2(\mathbf{G})}{2\,C_2(\mathbf{R})}\left(\dfrac{\alpha_s^{\rm NA}}{\alpha_s^B}\right)\right]^2, & [\mathbf{adj}]\to[\mathbf{1}], \\ \left[1 - \dfrac{C_2(\mathbf{G})}{2C_2(\mathbf{R}) - C_2(\mathbf{G})}\left(\dfrac{\alpha_s^{\rm NA}}{\alpha_s^B}\right)\right]^2, & [\mathbf{1}]\to[\mathbf{adj}], \\ d_{\mathbf{R}}^2(\eta_1^2+\eta_2^2) - 2 + C_2(\mathbf{G})\left[d_{\mathbf{R}}C(\mathbf{R}) - \dfrac{C_2(\mathbf{G})}{2}\right]\left(\dfrac{\alpha_s^{\rm NA}}{\alpha_g^B}\right)^2, & \mathbf{rest}, \end{cases} \tag{2.42b}$$

JHEP07(2018)096

and

$$S_{\rm BSF}(\zeta_S,\zeta_B) \equiv \left(\frac{2\pi\zeta_S}{1-e^{-2\pi\zeta_S}}\right)(1+\zeta_S^2)\left[\frac{\zeta_B^4\ \exp\left[-4\,\zeta_S\ \mathrm{arccot}(\zeta_B)\right]}{(1+\zeta_B^2)^3}\right]. \tag{2.42c}$$

A few remarks are in order:

- Clearly, in the [**adj**] → [**1**] transition, the contributions from all three diagrams of figure 1b add up. No (partial) cancellation occurs, for any group or representation, contrary to what was found in [55, 56]. We note that our result reproduces the dissociation rate via gluon absorption of the colour-singlet bound state of a particle-antiparticle pair transforming in the (anti)fundamental of SU(N), that was computed in ref. [61, eq. (19)].[5]

  The potential in the singlet state is always attractive and gives rise to the tightest bound state. Thus, our results quite generally suggest that BSF can be very significant for phenomenology.[6]

  Moreover, the radiative transitions contribute to the self-energy of the initial state. From the optical theorem and eq. (2.42b), it follows that the forward scattering amplitude (or equivalently, the index of refraction) of the adjoint state is enhanced by the non-Abelian contribution, as is reasonable to expect.

- Since α_s runs only logarithmically, to a good approximation we may set $\alpha_s^{\rm NA} \simeq \alpha_s^B$, at least in the parameter space where BSF is significant (cf. footnote 4). Then, for the [**adj**] → [**1**] and [**1**] → [**adj**] transitions, the f_c factors simplify.

- We recall that the couplings $\alpha_s^{\rm BSF}$, $\alpha_s^{\rm NA}$, α_s^B, α_g^B, α_g^S, and thus ζ_S and ζ_B, depend on the colour representations of the initial and final states (cf. table 1), and are different for every transition.

- As noted in section 2.4.3, if the group algebra allows for more than one transitions in the category "rest", then their contributions to f_c have to be disentangled, in order for $S_{\rm BSF}$ to be computed. Note that a transition $(XX^\dagger)_{\hat{\mathbf{R}}} \to (XX^\dagger)_{\hat{\mathbf{R}}'} + g$ allowed by the group algebra contributes to f_c even if $\hat{\mathbf{R}}'$ has a repulsive potential and cannot accommodate a bound state.

The function $S_{\rm BSF}(\zeta_S,\zeta_B)$ encapsulates all the velocity dependence of $\sigma_{\rm BSF}v_{\rm rel}$. The first two factors in eq. (2.42c) arise solely from the scattering-state wavefunction and coincide with the Coulomb Sommerfeld enhancement of p-wave annihilation processes $S_1(\zeta_S) = [2\pi\zeta_S/(1-e^{-2\pi\zeta_S})](1+\zeta_S^2)$. The factors inside the square brackets in eq. (2.42c) arise from the convolution of the scattering-state and bound-state wavefunctions with the radiative vertices.

[5] The gluo-dissociation ([61, eq. (19)]) and the radiative capture cross-sections [eqs. (2.42)] are related via the Milne relation, which we review in appendix D and use in section 3. Note that the gluo-dissociation cross-section of [61, eq. (19)] is not averaged over the gluon degrees of freedom, while $\sigma_{\rm ion}$ in eq. (D.4) is.

[6] For particle-antiparticle pairs transforming in the (anti)fundamental SU(N), the opposite relative sign between the Abelian and non-Abelian contributions leads to an accidental near cancellation and thus a suppression of the adjoint-to-singlet capture cross-section by a factor of $(2N^2-1)^2$.

JHEP07(2018)096

Let us now discuss the asymptotic behaviour of $S_{\rm BSF}$ in various cases.

- At large velocities, $|\zeta_S|, \zeta_B \ll 1$, BSF is very suppressed,

$$S_{\rm BSF} \simeq \zeta_B^4 \ll 1. \tag{2.43a}$$

- For an attractive interaction in the scattering state ($\zeta_S > 0$), and at low enough $v_{\rm rel}$ such that $\zeta_S \gtrsim 1$ and $\zeta_B \gtrsim 1$,

$$S_{\rm BSF} \simeq 2\pi\zeta_S \times \left(\frac{\zeta_S}{\zeta_B}\right)^2 \exp\left(-\frac{4\zeta_S}{\zeta_B}\right). \tag{2.43b}$$

  Since $\zeta_S/\zeta_B = \alpha_g^S/\alpha_g^B$ is constant, $S_{\rm BSF}$ exhibits the characteristic scaling $S_{\rm BSF} \propto 1/v_{\rm rel}$.[7] We observe that $S_{\rm BSF}$ becomes maximal for $\alpha_g^S/\alpha_g^B = 0.5$. That is, the transition probability decreases for transitions between states governed by very different potentials ($\alpha_g^S/\alpha_g^B \gg 1$ or $\ll 1$).

- For a repulsive interaction in the scattering state ($\zeta_S < 0$), and at low enough $v_{\rm rel}$ such that $\zeta_S \lesssim -1$ and $\zeta_B \gtrsim 1$,

$$S_{\rm BSF} \simeq 2\pi|\zeta_S| \left(\frac{\zeta_S}{\zeta_B}\right)^2 \exp\left[\left(\frac{4}{\zeta_B} - 2\pi\right)|\zeta_S|\right]. \tag{2.43c}$$

  At low $v_{\rm rel}$, $S_{\rm BSF}$ becomes exponential suppressed. However, the exponential suppression sets at $\zeta_B > 1$, by when BSF may already have an important effect on the DM density. It is interesting that the exponential suppression is more severe for tighter bound states (larger ζ_B), i.e. two particles that repel each other are less likely to be captured into a very deep bound state. This is consistent with the behaviour exhibited by eq. (2.43b).

3 Dark matter co-annihilating with coloured partners

3.1 Simplified model and Boltzmann equation

We assume that DM is a Majorana fermion χ of mass m_χ, that co-annihilates with a complex scalar triplet under $\mathrm{SU}(3)_c$, denoted by X. The gauge interactions of X are specified by the Lagrangian

$$\delta\mathcal{L} = (D_{\mu,ij}X_j)^\dagger \left(D^\mu_{ij'}X_{j'}\right) - m_X^2\, X_j^\dagger X_j\,, \tag{3.1}$$

where $D_{\mu,ij} = \delta_{ij}\partial_\mu + ig_s\, G_\mu^a T_{ij}^a$ is the covariant derivative, with G_μ^a being the gluon fields and T^a are the generators. χ and X are the lightest and next-to-lightest particles that are odd under a Z_2 symmetry which prevents χ from decaying. We also assume that the interactions between χ and X — which we shall leave unspecified — keep them in chemical equilibrium throughout the freeze-out of their annihilation processes into other species.

[7] This scaling appears also in the upper limit on inelastic cross-sections imposed by unitarity. This implies that the unitarity limit may be approached or realised only by Sommerfeld enhanced processes [4, 5].

JHEP07(2018)096

As long as the relative mass splitting between DM and its coannihilating partner,

$$\delta \equiv (m_X - m_\chi)/m_\chi \,, \tag{3.2}$$

is small, $\delta \ll 1$, the DM density is determined by the $\chi - \chi$, $\chi - X$, $\chi - X^\dagger$ and $X - X^\dagger$ (co-)annhilation processes. It can be tracked by considering the sum of densities of all co-annihilating species,

$$\tilde{Y} \equiv Y_\chi + Y_X + Y_{X^\dagger} = Y_\chi + 2Y_X \,, \tag{3.3}$$

where $Y_j \equiv n_j/s$, with n_j being the number density of the species j and $s \equiv (2\pi^2/45)\, g_{*S}\, T^3$ being the entropy density of the universe. Using the time parameter

$$x \equiv m_\chi/T, \tag{3.4}$$

the evolution of $\tilde{Y}$ is governed by the Boltzmann equation [67]

$$\frac{d\tilde{Y}}{dx} = -\frac{c\, g_{*,\mathrm{eff}}^{1/2}\, \langle \sigma_{\mathrm{eff}}\, v_{\mathrm{rel}} \rangle}{x^2} \, (\tilde{Y}^2 - \tilde{Y}_{\mathrm{eq}}^2) \,, \tag{3.5a}$$

where

$$c \equiv \sqrt{\pi/45}\; m_{\mathrm{Pl}} m_\chi \,, \tag{3.5b}$$

$$g_{*,\mathrm{eff}}^{1/2} \equiv \frac{g_{*S}}{\sqrt{g_*}} \left(1 + \frac{T}{3 g_{*S}} \frac{d g_{*S}}{dT} \right) , \tag{3.5c}$$

$$Y_\chi^{\mathrm{eq}} = \frac{90}{(2\pi)^{7/2}} \, \frac{g_\chi}{g_{*S}} \, x^{3/2} \, e^{-x} \,, \tag{3.5d}$$

$$Y_X^{\mathrm{eq}} = Y_{X^\dagger}^{\mathrm{eq}} = \frac{90}{(2\pi)^{7/2}} \, \frac{g_X}{g_{*S}} \, [(1+\delta)x]^{3/2} \, e^{-(1+\delta)x} \,, \tag{3.5e}$$

with $g_\chi = 2$ and $g_X = 3$ being the χ and X degrees of freedom.

The *effective* cross-section $\langle \sigma_{\mathrm{eff}}\, v_{\mathrm{rel}} \rangle$ in eq. (3.5a) includes all annihilation and co-annihilation processes weighted by the densities of the participating species. We shall assume that the dominant contribution arises from the processes that annihilate $XX^\dagger$, with total cross-section $\sigma_{XX^\dagger}$, such that

$$\langle \sigma_{\mathrm{eff}}\, v_{\mathrm{rel}} \rangle = \frac{2 Y_X^{\mathrm{eq}} Y_{X^\dagger}^{\mathrm{eq}} \, \langle \sigma_{XX^\dagger}\, v_{\mathrm{rel}} \rangle}{\tilde{Y}_{\mathrm{eq}}^2} = \langle \sigma_{XX^\dagger}\, v_{\mathrm{rel}} \rangle \left(\frac{2 g_X^2 (1+\delta)^3 \, e^{-2x\,\delta}}{\left[g_\chi + 2 g_X (1+\delta)^{3/2} \, e^{-x\,\delta} \right]^2} \right) . \tag{3.6}$$

Both the direct annihilation and the BSF processes contribute to $\sigma_{XX^\dagger}$, as we discuss in the following.

In this work, we shall neglect thermal effects. The thermal bath may affect the DM freeze-out in a variety of ways, including, on one hand, screening of the long-range interactions and, on the other hand, frequent (non-radiative) scattering processes that precipitate DM depletion via BSF [49]. In the context of DM coannihilation with coloured partners, the latter have been considered in ref. [51]. The inclusion of thermal corrections for the radiative BSF processes considered here requires a comprehensive study that we leave for future work.

JHEP07(2018)096

Vertices	$\boldsymbol{\alpha_s}$	$\boldsymbol{\alpha_g}$	**Average momentum transfer $\boldsymbol{Q}$**
Annihilation: gluon emission	$\alpha_s^{\rm ann}$		m_X
Scattering-state wavefunctions	α_s^S	Colour singlet $\alpha^S_{g,[\mathbf{1}]} = 4\alpha_s^S/3$	$\dfrac{m_X\, v_{\rm rel}}{2}$
		Colour octet $\alpha^S_{g,[\mathbf{8}]} = -\alpha_s^S/6$	
Colour-singlet bound-state wavefunction	$\alpha^B_{s,[\mathbf{1}]}$	$\alpha^B_{g,[\mathbf{1}]} = \dfrac{4\alpha^B_{s,[\mathbf{1}]}}{3}$	$\dfrac{m_X}{2}\left(\dfrac{4\alpha^B_{s,[\mathbf{1}]}}{3}\right)$
Colour-singlet bound-state formation: gluon emission	$\alpha^{\rm BSF}_{s,[\mathbf{1}]}$		$\dfrac{m_X}{4}\left[v_{\rm rel}^2 + \left(\dfrac{4\alpha^B_{s,[\mathbf{1}]}}{3}\right)^2\right]$
$gX^\dagger X$ vertices in non-Abelian diagram for colour-singlet BSF	$\alpha^{\rm NA}_{s,[\mathbf{1}]} \approx \alpha^B_{s,[\mathbf{1}]}$		$(m_X/2)\sqrt{v_{\rm rel}^2 + {\alpha^B_{g,[\mathbf{1}]}}^2}$ approximated with $(m_X/2)\alpha^B_{g,[\mathbf{1}]}$

Table 2. The momentum transfer Q at which the strong coupling $\alpha_s(Q)$ is evaluated, for the various processes and the states participating in these processes, in the model of section 3.

3.2 Colour states and the running of the coupling

The $X - X^\dagger$ colour interaction may be decomposed as

$$\mathbf{3} \otimes \bar{\mathbf{3}} = \mathbf{1} \oplus \mathbf{8}\,. \tag{3.7}$$

In each irreducible representation $\hat{\mathbf{R}}$, the gluon exchange gives rise to the Coulomb potential of eq. (2.13) with the coupling α_g given by eq. (2.14). The quadratic Casimir invariants for the SU(3) representations of interest are $C_2(\mathbf{1}) = 0$, $C_2(\mathbf{3}) = C_2(\bar{\mathbf{3}}) = 4/3$, $C_2(\mathbf{8}) = 3$, therefore

$$\alpha_g \equiv \alpha_s \times \begin{cases} 4/3, & \hat{\mathbf{R}} = \mathbf{1}, \\ -1/6, & \hat{\mathbf{R}} = \mathbf{8}. \end{cases} \tag{3.8}$$

As discussed in section 2.2, the strong coupling α_s depends on the momentum transfer Q. In table 2, we list the average Q for the various vertices appearing in the annihilation and BSF processes, in this model. For the bound states, the momentum transfer depends itself on the strong coupling, $Q = Q(\alpha_s)$. In this case, we determine α_s by solving the numerically the equation

$$\alpha_s(Q(\tilde{\alpha})) = \tilde{\alpha}\,, \tag{3.9}$$

for $\tilde{a}$. We discuss further the effect of the α_s running in the following.

JHEP07(2018)096

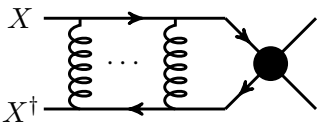

(a) The $XX^\dagger$ annihilation is influenced by the Sommerfeld effect due to gluon exchange. The black blob represents the perturbative part of the annihilation processes (hard scattering).

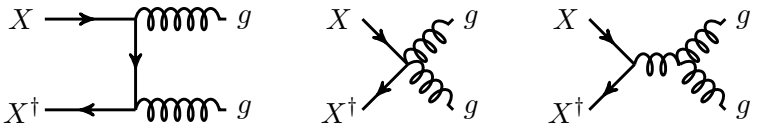

(b) Tree-level diagrams contributing to the hard process $XX^\dagger \to gg$. Besides the t-channel diagram, there is the corresponding u-channel (not shown). The s-channel yields a p-wave contribution, which we neglect.

Figure 2. $XX^\dagger$ annihilation into gluons.

3.3 Direct annihilation

$XX^\dagger$ pairs annihilate dominantly into gluons (cf. figure 2), with cross-section [68]

$$\sigma_{XX^\dagger\to gg} v_{\rm rel} = \frac{14}{27}\frac{\pi(\alpha_s^{\rm ann})^2}{m_X^2} \times \left(\frac{2}{7}S_{0,[\mathbf{1}]} + \frac{5}{7}S_{0,[\mathbf{8}]}\right) , \tag{3.10}$$

where $S_{0,[\mathbf{1}]}$ and $S_{0,[\mathbf{8}]}$ are the s-wave Sommerfeld factors of the colour-singlet and colour-octet states,

$$S_{0,[\mathbf{1}]} \equiv S_0\left(\frac{4\alpha_s^S}{3v_{\rm rel}}\right) \qquad \text{and} \qquad S_{0,[\mathbf{8}]} \equiv S_0\left(-\frac{\alpha_s^S}{6v_{\rm rel}}\right) . \tag{3.11}$$

The function $S_0(\zeta_S)$ is the s-wave Sommerfeld enhancement factor (cf. ref. [69] and appendix A),

$$S_0(\zeta_S) \equiv \frac{2\pi\zeta_S}{1-e^{-2\pi\zeta_S}} . \tag{3.12}$$

The annihilation $XX^\dagger \to q\bar{q}$ is p-wave suppressed and we neglect it for simplicity. In figure 3, we show $S_0(\zeta_S)$, for both attractive and repulsive interactions, and depict the effect of the α_s running on the Sommerfeld factors. Because the momentum exchange in the scattering state is much smaller than on the gluon-emission vertices (cf. table 2), α_s^S is considerably larger than $\alpha_s^{\rm ann}$, as seen in the top right panel of figure 3.

3.4 Bound-state formation, ionisation and decay

Formation. As seen from eq. (3.8), only the colour-singlet $XX^\dagger$ state interacts via an attractive potential and can form bound states. The only capture process via one-gluon emission is from the octet state,

$$(X + X^\dagger)_{[\mathbf{8}]} \to \mathcal{B}(XX^\dagger)_{[\mathbf{1}]} + g_{[\mathbf{8}]} . \tag{3.13}$$

JHEP07(2018)096

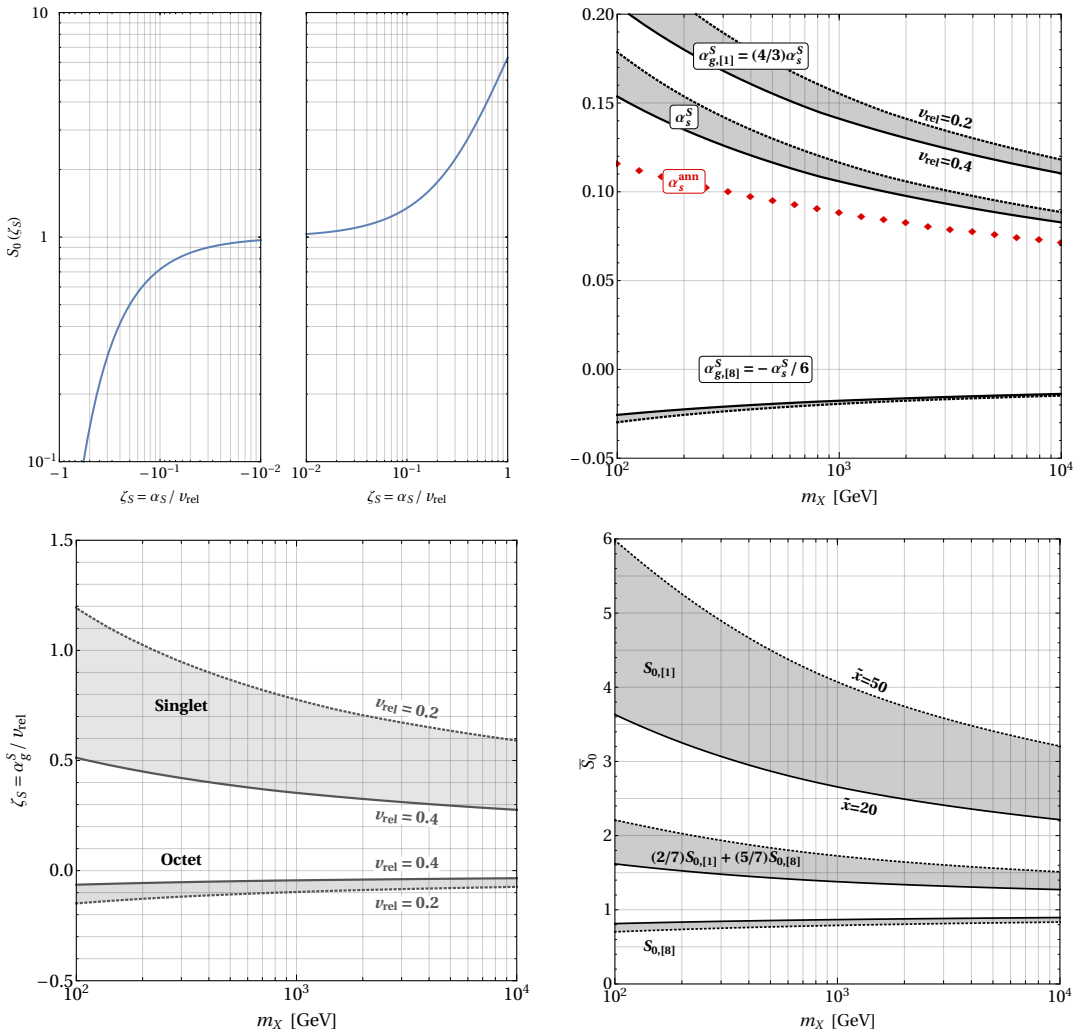

Figure 3. *Top left:* the Sommerfeld factor for s-wave annihilation, $S_0(\zeta_S)$, vs $\zeta_S \equiv \alpha_g^S/v_{\rm rel}$, for both attractive ($\zeta_S > 0$) and repulsive ($\zeta_S < 0$) Coulomb interaction. *Top right:* the running of α_s in the scattering states, where the average momentum exchange is $Q = (m_X/2)v_{\rm rel}$. For the colour-singlet and the colour-octet states, $\alpha^S_{g,[1]} = (4/3)\alpha^S_s$ and $\alpha^S_{g,[8]} = -\alpha^S_s/6$. We show α^S_s, $\alpha^S_{g,[1]}$ and $\alpha^S_{g,[8]}$ in the velocity range $0.2 < v_{\rm rel} < 0.4$, that is typical during the DM freeze-out. For comparison, we also show the strong coupling at the gluon emission vertices of the annihilation processes, $\alpha_s^{\rm ann}$, which corresponds to $Q = m_X$ (*red diamonds*). *Bottom left:* the parameter $\zeta_S = \alpha_g^S/v_{\rm rel}$ that determines the Sommerfeld effect. *Bottom right:* the thermally-averaged s-wave Sommerfeld factor, $\bar{S}_0$, for $\tilde{x} \equiv m_X/T$ within the indicative range $20 < \tilde{x} < 50$ during which the DM abundance freezes-out.

Using $d_{\mathbf{R}} = 3$, $C(\mathbf{3}) = 1/2$, $C_2(\mathbf{3}) = 4/3$ and $C_2(\mathbf{G}) = 3$, and setting $\eta_1 = \eta_2 = 1/2$ and $\mu = m_X/2$, we find from eqs. (2.42) the colour-averaged BSF cross-section,

$$\sigma^{[\mathbf{8}]\to[\mathbf{1}]}_{\rm BSF} v_{\rm rel} = \frac{2^7 17^2}{3^5} \frac{\pi \alpha_s^{\rm BSF} \alpha^B_{s,[1]}}{m_X^2} \times S_{\rm BSF}(\zeta_S, \zeta_B)\,, \tag{3.14}$$

where $S_{\rm BSF}(\zeta_S, \zeta_B)$ is given by eq. (2.42c), and here $\zeta_S = \alpha^S_{g,[\mathbf{8}]}/v_{\rm rel}$, $\zeta_B = \alpha^B_{g,[\mathbf{1}]}/v_{\rm rel}$ [cf. eqs. (2.41)].

JHEP07(2018)096

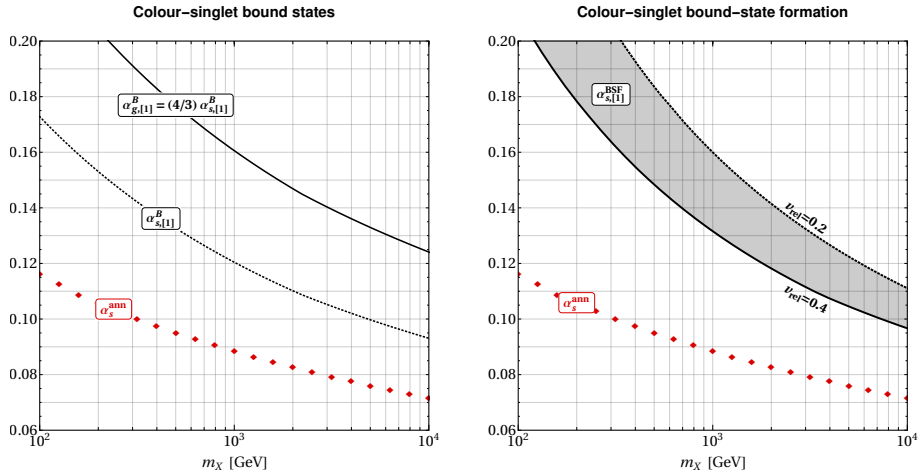

Figure 4. *Left panel*: the strong coupling $\alpha^B_{s,[\mathbf{1}]}$ and the corresponding $\alpha^B_{g,[\mathbf{1}]}$, that determine the colour-singlet bound-state wavefunction. *Right panel*: the strong coupling at the gluon emission vertex during the formation of colour-singlet bound states, $\alpha^{\rm BSF}_{s,[\mathbf{1}]}$. The emitted gluon carries away the binding energy of the bound state plus the kinetic energy of the scattering state; we show $\alpha^{\rm BSF}_{s,[\mathbf{1}]}$ in the range $0.2 \leqslant v_{\rm rel} \leqslant 0.4$ that is indicative of the relative velocities during DM freeze-out.

The coupling $\alpha^B_{s,[\mathbf{1}]}$ that determines the bound-state wavefunction, and the coupling $\alpha^{\rm BSF}_{s,[\mathbf{1}]}$ that corresponds to the gluon radiation vertex in the capture process, are shown in figure 4. Due to the small momentum transfer (cf. table 2), they are considerably larger than $\alpha_s^{\rm ann}$ that corresponds to the gluon vertices in the $XX^\dagger \to gg$ annihilation. This enhances further the BSF cross-section with respect to the annihilation cross-section, as seen by comparing the two panels in figure 5.

In figure 5, we compare eq. (3.14) to the cross-section for $XX^\dagger \to gg$ (cf. eq. (3.10)). At large velocities, $\alpha_s/v_{\rm rel} \ll 1$, the BSF cross-section scales as $\sigma^{[\mathbf{8}]\to[\mathbf{1}]}_{\rm BSF} v_{\rm rel} \propto (\alpha_s/v_{\rm rel})^4$ and is subdominant to annihilation. At low velocities, $\alpha_s/v_{\rm rel} \gg 1$, it becomes exponentially suppressed due to the Coulomb repulsion in the scattering state. $\sigma^{[\mathbf{8}]\to[\mathbf{1}]}_{\rm BSF} v_{\rm rel}$ peaks at $\alpha_s/v_{\rm rel} \approx 1$, where it exceeds the annihilation cross-section by more than one order of magnitude.

The thermally-averaged BSF cross-section is

$$\langle \sigma^{[\mathbf{8}]\to[\mathbf{1}]}_{\rm BSF} v_{\rm rel} \rangle = \left(\frac{\mu}{2\pi T}\right)^{3/2} \int d^3 v_{\rm rel}\ \exp\left(-\frac{\mu v_{\rm rel}^2}{2T}\right) [1 + f_g(\omega)]\ \sigma^{[\mathbf{8}]\to[\mathbf{1}]}_{\rm BSF} v_{\rm rel}\,, \tag{3.15}$$

where $\mu = m_X/2$ is the $X - X^\dagger$ reduced mass. Here, $f_g(\omega) = 1/(e^{\omega/T} - 1)$ is the gluon occupation number, with ω being the energy of the emitted gluon,

$$\omega = \frac{\mu}{2}[(\alpha^B_g)^2 + v_{\rm rel}^2]\,. \tag{3.16}$$

The factor $1 + f_g(\omega)$ accounts for the Bose enhancement due to the final-state gluon, and is necessary to ensure the detailed balance between the bound-state formation and ionisation processes at $T \gtrsim \omega$ [4], which encompasses a significant temperature range that is relevant to the DM freeze-out.

JHEP07(2018)096

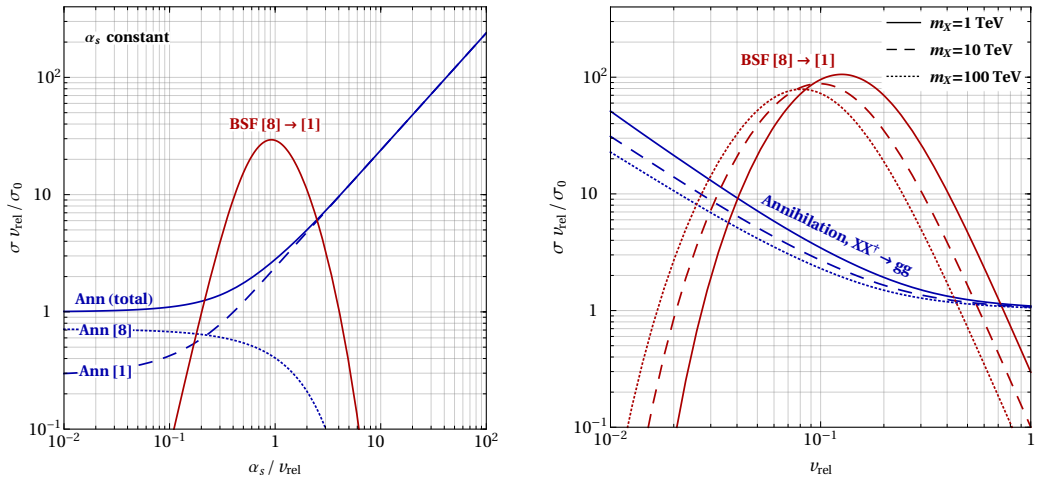

Figure 5. *Left*: the cross-sections times relative velocity for annihilation into gluons, $XX^\dagger \to gg$ (*blue lines*), and radiative capture into the ground state (*red line*), normalised to the perturbative annihilation cross-section times relative velocity $\sigma_0 \equiv 14\pi\alpha_s^2/(27m_X^2)$. The *blue dashed* and *blue dotted* lines denote the contributions of the colour-singlet and the colour-octet scattering states in the total annihilation cross-section. We have ignored here the running of the strong coupling, which implies that $\sigma v_{\rm rel}/\sigma_0$ depend only on $\alpha_s/v_{\rm rel}$. *Right*: the cross-sections times relative velocity for annihilation into gluons, $XX^\dagger \to gg$ (*blue lines*), and radiative capture into the ground state (*red line*), normalised to σ_0. The lines corresponding to different values of m_x differ due to the running of the strong coupling.

Ionisation. The ionisation and BSF cross-sections are related via the Milne relation, which we review in appendix D. From eq. (D.4), we find

$$\sigma_{\rm ion} = \frac{g_X^2}{g_g g_{\mathcal{B}}} \left(\frac{\mu^2 v_{\rm rel}^2}{\omega^2}\right) \sigma_{\rm BSF}\,, \tag{3.17}$$

where g_g and $g_{\mathcal{B}}$ are the gluon and bound-state degrees of freedom. The ionisation rate is

$$\Gamma_{\rm ion} = g_g \int_{\omega_{\rm min}}^{\infty} \frac{d\omega}{2\pi^2} \frac{\omega^2}{e^{\omega/T}-1}\, \sigma_{\rm ion}\,.$$

Using eqs. (3.16) and (3.17), we obtain the ionisation rate of the colour-singlet bound states,

$$\Gamma_{{\rm ion},[\mathbf{1}]} = \frac{g_X^2 \mu^3}{2\pi^2 g_{\mathcal{B},[\mathbf{1}]}} \int_0^\infty dv_{\rm rel}\, \frac{v_{\rm rel}^2}{\exp\left\{\dfrac{\mu[(\alpha^B_{g,[\mathbf{1}]})^2 + v_{\rm rel}^2]}{2T}\right\} - 1}\, \sigma_{\rm BSF}^{[\mathbf{8}]\to[\mathbf{1}]} v_{\rm rel}\,. \tag{3.18}$$

We compute (3.18) using $g_g = 8$, $g_X = 3$, $g_{\mathcal{B},[\mathbf{1}]} = 1$, $\mu = m_X/2$ and eq. (3.14).

Decay. The decay rate of $\ell = 0$ bound states is related to the perturbative s-wave annihilation cross-section times relative velocity of the corresponding scattering states (see e.g. [57]),

$$\Gamma_{\rm dec} = (\sigma^{s-{\rm wave}}_{{\rm ann},[\hat{\mathbf{R}}]} v_{\rm rel})\; |\psi^{[\hat{\mathbf{R}}]}_{n\ell m}(0)|^2\,. \tag{3.19}$$

JHEP07(2018)096

Note that $\sigma^{s-\text{wave}}_{\text{ann},[\hat{\mathbf{R}}]} v_{\text{rel}}$ corresponds to the colour configuration of the bound state and should be averaged over the bound-state colour degrees of freedom, rather than those of an unbound $XX^\dagger$ pair.

For the colour-singlet states (cf. eq. (3.10), noting that $g_X^2 = 9$ and $g_{[\mathbf{1}]} = 1$)

$$\sigma^{s-\text{wave}}_{\text{ann},[\mathbf{1}]} v_{\text{rel}} = \frac{4\pi(\alpha_s^{\text{ann}})^2}{3m_X^2} \,. \tag{3.20}$$

The colour-singlet ground-state wavefunction at the origin is [cf. eq. (A.9)]

$$|\psi^{[\mathbf{1}]}_{1,0,0}(0)|^2 = \frac{\mu^3(\alpha^B_{g,[\mathbf{1}]})^3}{\pi} = \frac{2^3 m_X^3 (\alpha^B_{s,[\mathbf{1}]})^3}{3^3\pi} \,. \tag{3.21}$$

Thus, the decay rate of the colour-singlet ground state is

$$\Gamma_{\text{dec},[\mathbf{1}]} = \frac{32}{81}\, m_X\, (\alpha_s^{\text{ann}})^2 (\alpha^B_{s,[\mathbf{1}]})^3 \,. \tag{3.22}$$

Effective bound-state formation cross-section. The effect of unstable bound states on the DM relic density is governed by a system of coupled Boltzmann equations for the unbound and bound particles that describe the interplay between bound-state formation, ionisation and decay processes [4]. However, it is possible to incorporate the effect of bound states in a single Boltzmann equation for the unbound particles, using an effective BSF cross-section that is weighted by the fraction of bound states that decay (rather than getting ionised),

$$\langle \sigma_{\text{BSF}} v_{\text{rel}} \rangle_{\text{eff}} \equiv \langle \sigma^{[\mathbf{8}]\to[\mathbf{1}]}_{\text{BSF}} v_{\text{rel}} \rangle \times \left(\frac{\Gamma_{\text{dec},[\mathbf{1}]}}{\Gamma_{\text{dec},[\mathbf{1}]} + \Gamma_{\text{ion},[\mathbf{1}]}} \right) . \tag{3.23}$$

3.5 Relic density

The total cross-section of the processes that deplete $XX^\dagger$ is

$$\langle \sigma_{XX^\dagger}\, v_{\text{rel}} \rangle = \langle \sigma_{XX^\dagger \to gg}\, v_{\text{rel}} \rangle + \langle \sigma_{\text{BSF}}\, v_{\text{rel}} \rangle_{\text{eff}} \,, \tag{3.24}$$

where the individual cross-sections are given in eqs. (3.10) and (3.23). From eqs. (3.6) and (3.24), we obtain $\langle \sigma_{\text{eff}}\, v_{\text{rel}} \rangle$ which enters the Boltzmann eq. (3.5a). In figure 6, we show $\langle \sigma_{\text{eff}}\, v_{\text{rel}} \rangle$ as a function of the time parameter m_X/T, together with the contributions it receives from direct annihilation and from BSF. At early times, the depletion of DM via BSF is impeded by the large ionisation rate of the bound states. However, BSF becomes more efficient than direct annihilation in depleting DM at $m_X/T \gtrsim 70$ for $m_X \sim$ TeV, suggesting that a sizeable effect on the DM density should be expected.

In figure 7 we present the results of the relic density computation. In the left panel, we show the mass splitting $\Delta m \equiv m_X - m_\chi$ vs. m_χ, in three different cases, (i) considering perturbative annihilation only, (ii) taking into account the Sommerfeld effect on the direct annihilation processes, and (iii) including the formation and decay of unstable bound states. In agreement with previous works [33, 38], we confirm that the Sommerfeld effect has a considerable impact on the predicted Δm and m_χ. In addition, we find that BSF has

JHEP07(2018)096

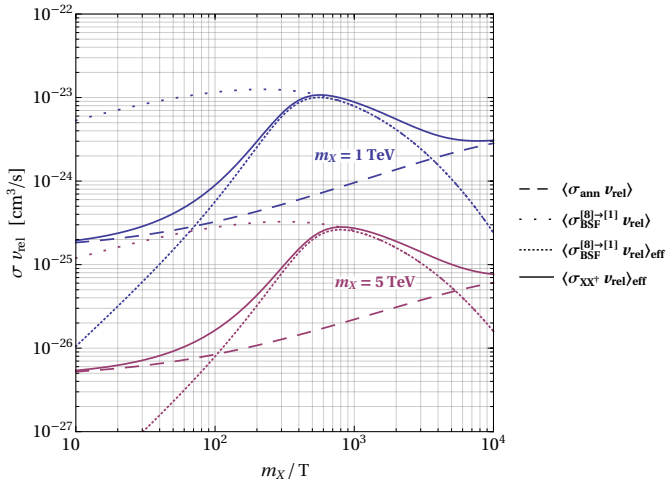

Figure 6. *Dashed lines:* the thermally averaged cross-section for annihilation into gluons, $XX^\dagger \to gg$ [cf. eq. (3.10)]. *Wide-spaced dotted lines:* the thermally averaged cross-section for the radiative capture into the colour-singlet bound state [cf. eq. (3.15)]. *Densely spaced dotted lines:* the effective bound-state formation cross-section, which is weighted by the fraction of $XX^\dagger$ pairs that decay into radiation, rather than getting ionised [cf. eq. (3.23)]. *Solid lines:* the total effective cross-section of processes that deplete $XX^\dagger$ pairs [cf. eq. (3.24)]. This determines the DM effective annihilation cross-section via eq. (3.6).

a significant effect. It implies that the mass splitting can be as high as ~ 38 GeV, and DM can be as heavy as 3.3 TeV. For the viable m_χ and Δm values determined by the full computation, we show in the right panel of figure 7, the depletion of DM due to the Sommerfeld enhancement of the direct annihilation and due to BSF. We find that BSF depletes DM by (40–240)%. Clearly, this far exceeds the experimental uncertainty on the DM density.

4 Conclusion

Long-range interactions imply that non-perturbative effects and a variety of radiative processes come into play. Here, we have considered the radiative capture of non-relativistic particles into bound states, in unbroken non-Abelian gauge theories, in the regime where the gauge coupling is perturbative. This can be important in multi-TeV WIMP DM scenarios, in scenarios where DM co-annihilates with coloured particles, as well as in hidden sector models.

Our main results include the amplitude for the radiative formation of bound states via one-gluon emission, for arbitrary representations and masses of the interacting particles [cf. eq. (2.25)], and the complete BSF cross-sections for particles transforming in conjugate representations [cf. eqs. (2.42)], but still for arbitrary masses.

As a first application of our results, we considered a simplified model where DM coannihilates with particles transforming in the fundamental of $\mathrm{SU}(3)_c$, and showed that the formation and decay of particle-antiparticle bound states can affect the DM relic density

JHEP07(2018)096

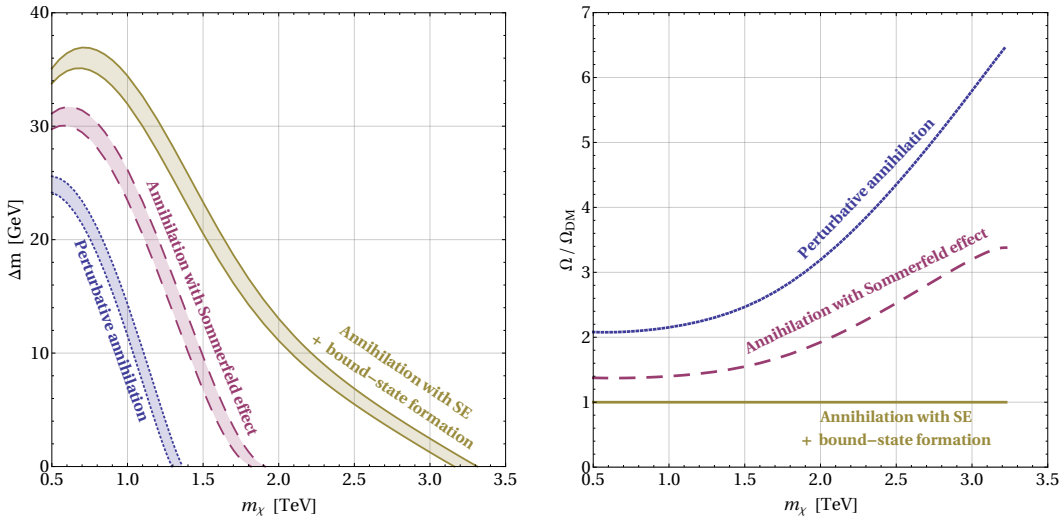

Figure 7. *Left panel:* the mass splitting Δm between DM and its coloured co-annihilating partner, that is required to obtain the observed DM density. The *blue dotted band* takes into account perturbative annihilation only, the *purple dashed band* incorporates the Sommerfeld effect on the direct annihilation, and the *yellow solid band* includes also the effect of bound-state formation and decay. The width of the bands arises from the 3σ uncertainty on the DM density. *Right panel:* the impact of the Sommerfeld effect and bound-state formation on the DM density. Δm is fixed with respect to m_χ along the yellow solid band of the left panel. We present the ratios of the relic densities predicted by perturbative annihilation only (blue dotted line) and by Sommerfeld-enhanced annihilation (purple dashed line), to the relic density predicted by the full computation that includes the effect of bound states.

very significantly. This implies larger DM mass and/or mass splitting between DM and its coannihilating particles, thereby altering the interpretation of the experimental results, and affecting the detection prospects. In particular, larger mass splittings imply the production of harder jets that can be more easily probed in collider experiments. Moreover, larger DM masses motivate indirect searches in the multi-TeV regime.

While the analytical formulae (2.42) assume a Coulomb potential, it is straightforward to generalise our results to other potentials, by computing the overlap integrals (2.26) using the wavefunctions arising from those potentials. This allows to include, for example, thermal masses for the gauge bosons, as well as the effect of multiple force mediators. The latter has been shown to be important in models where the (co-)annihilating particles possess a significant coupling to the Higgs [58, 70]. We leave these extensions for future work.

A Scattering-state and bound-state wavefunctions

The non-relativistic potentials due to gluon exchange, for the scattering and bound states are

$$V_{\rm scatt}(r) = -\alpha_g^S/r\,, \tag{A.1a}$$

$$V_{\rm bound}(r) = -\alpha_g^B/r\,. \tag{A.1b}$$

JHEP07(2018)096

where α_g^S may be either positive or negative, but $\alpha_g^B > 0$. The scattering and bound states are characterised by the momenta

$$\mathbf{k} \equiv \mu \mathbf{v}_{\rm rel}\,, \tag{A.2a}$$

$$\kappa \equiv \mu \alpha_g^B\,, \tag{A.2b}$$

where $\mathbf{v}_{\rm rel}$ is the expectation value of the relative velocity in the scattering state and κ is the Bohr momentum of the bound state. The corresponding wavefunctions, $\phi_{\mathbf{k}}(\mathbf{r})$ and $\psi_{n\ell m}(\mathbf{r})$, with $\{n, \ell, m\}$ being the principal and angular-momentum quantum numbers, obey the Schrödinger equations

$$\left[-\frac{\nabla^2}{2\mu} + V_{\rm scatt}(\mathbf{r})\right] \phi_{\mathbf{k}}(\mathbf{r}) = \mathcal{E}_{\mathbf{k}}\, \phi_{\mathbf{k}}(\mathbf{r})\,, \tag{A.3a}$$

$$\left[-\frac{\nabla^2}{2\mu} + V_{\rm bound}(\mathbf{r})\right] \psi_{n\ell m}(\mathbf{r}) = \mathcal{E}_{n\ell}\, \psi_{n\ell m}(\mathbf{r})\,, \tag{A.3b}$$

where

$$\mathcal{E}_{\mathbf{k}} \equiv \frac{\mathbf{k}^2}{2\mu} = \frac{1}{2}\mu v_{\rm rel}^2\,, \tag{A.4a}$$

$$\mathcal{E}_{n\ell} \equiv -\frac{\kappa^2}{2n^2\mu} = -\frac{1}{2n^2}\,\mu(\alpha_g^B)^2\,, \tag{A.4b}$$

The wavefunctions are normalised according to

$$\int d^3r\; \phi^*_{\mathbf{k}}(\mathbf{r})\, \phi_{\mathbf{k}'}(\mathbf{r}) = (2\pi)^3 \delta^3(\mathbf{k} - \mathbf{k}')\,. \tag{A.5a}$$

$$\int d^3r\; \psi^*_{n\ell m}(\mathbf{r})\, \psi_{n'\ell'm'}(\mathbf{r}) = \delta_{nn'}\delta_{\ell\ell'}\delta_{mm'}\,. \tag{A.5b}$$

For convenience, we shall define

$$\zeta_S \equiv \alpha_g^S / v_{\rm rel}\,, \tag{A.6a}$$

$$\zeta_B \equiv \alpha_g^B / v_{\rm rel}\,. \tag{A.6b}$$

and

$$S_0(\zeta_S) \equiv \frac{2\pi\zeta_S}{1 - e^{-2\pi\zeta_S}}\,. \tag{A.7}$$

The solutions to eqs. (A.3) with the potentials (2.13), are (see e.g. [71])

$$\phi_{\mathbf{k}}(\mathbf{r}) = \sqrt{S_0(\zeta_S)}\; {}_1F_1[i\zeta_S;\; 1;\; i(kr - \mathbf{k}\cdot\mathbf{r})]\; e^{i\mathbf{k}\cdot\mathbf{r}}\,. \tag{A.8a}$$

$$\psi_{n\ell m}(\mathbf{r}) = \kappa^{3/2}\; \left[\frac{4(n-\ell-1)!}{n^4(n+\ell)!}\right]^{1/2}\; \left(\frac{2\kappa r}{n}\right)^{\ell}\; L^{(2\ell+1)}_{n-\ell-1}\left(\frac{2\kappa r}{n}\right)\; e^{-\kappa r/n}\; Y_{\ell m}(\Omega_{\mathbf{r}})\,, \tag{A.8b}$$

where ${}_1F_1$ is the confluent hypergeometric function of the first kind, and L^a_n are the generalised Laguerre polynomials of degree n. (We assume the normalisation condition $\int_0^\infty z^a e^{-z} L_n^{(a)}(z) L_m^{(a)}(z) dz = [\Gamma(n+a+1)/n!]\delta_{n,m}$.) For the ground state, $\{n, \ell, m\} = \{1, 0, 0\}$,

$$\psi_{100}(\mathbf{r}) = \sqrt{\kappa^3/\pi}\; e^{-\kappa r}\,. \tag{A.9}$$

JHEP07(2018)096

Note that S_0 is the Sommerfeld factor for s-wave annihilation (see e.g. [69])

$$S_0(\zeta_S) = |\phi_{\mathbf{k}}(r=0)|^2 \,. \tag{A.10}$$

In section 2, we also need the Fourier transforms of the wavefunctions, defined as

$$\tilde{\phi}_{\mathbf{k}}(\mathbf{q}) = \int d^3r\ \phi_{\mathbf{k}}(\mathbf{r})\ e^{-i\mathbf{q}\,\mathbf{r}}\,, \qquad \phi_{\mathbf{k}}(\mathbf{r}) = \int \frac{d^3q}{(2\pi)^3}\ \tilde{\phi}_{\mathbf{k}}(\mathbf{q})\ e^{i\mathbf{q}\,\mathbf{r}}\,, \tag{A.11a}$$

$$\tilde{\psi}_{n\ell m}(\mathbf{p}) = \int d^3r\ \psi_{n\ell m}(\mathbf{r})\ e^{-i\mathbf{p}\,\mathbf{r}}\,, \qquad \psi_{n\ell m}(\mathbf{r}) = \int \frac{d^3p}{(2\pi)^3}\ \tilde{\psi}_{n\ell m}(\mathbf{p})\ e^{i\mathbf{p}\,\mathbf{r}}\,. \tag{A.11b}$$

B Overlap integrals for capture into the ground state

For the BSF cross-sections of interest, we need to compute the overlap integrals defined in eqs. (2.26). In coordinate space, they become

$$\boldsymbol{\mathcal{J}}_{\mathbf{k},\{n\ell m\}}(\mathbf{b}) \equiv \int \frac{d^3p}{(2\pi)^3}\ \mathbf{p}\,\tilde{\psi}^*_{n\ell m}(\mathbf{p})\,\tilde{\phi}_{\mathbf{k}}(\mathbf{p}+\mathbf{b}) = i\int d^3r\ [\nabla\psi^*_{n\ell m}(\mathbf{r})]\,\phi_{\mathbf{k}}(\mathbf{r})\ e^{-i\mathbf{b}\mathbf{r}}\,, \tag{B.1a}$$

$$\begin{aligned}\boldsymbol{\mathcal{Y}}_{\mathbf{k},\{n\ell m\}} &\equiv 8\pi\mu\alpha_s^{\rm NA}\int \frac{d^3p}{(2\pi)^3}\frac{d^3q}{(2\pi)^3}\frac{\mathbf{q}-\mathbf{p}}{(\mathbf{q}-\mathbf{p})^4}\,\tilde{\psi}^*_{n\ell m}(\mathbf{p})\,\tilde{\phi}_{\mathbf{k}}(\mathbf{q}) \\ &= -i\mu\alpha_s^{\rm NA}\int d^3r\,\psi^*_{n\ell m}(\mathbf{r})\,\phi_{\mathbf{k}}(\mathbf{r})\,\hat{\mathbf{r}}\,.\end{aligned} \tag{B.1b}$$

In deriving eq. (B.1b), we Fourier-transformed $\tilde{\psi}^*_{n\ell m}(\mathbf{p})$ and $\tilde{\phi}_{\mathbf{k}}(\mathbf{q})$, and used the following integral in the limit $m_g \to 0$,

$$\begin{aligned}\int \frac{d^3q}{(2\pi)^3}\ \frac{\mathbf{q}\,e^{-i\mathbf{q}\mathbf{r}}}{(\mathbf{q}^2+m_g^2)^2} &= i\,\nabla_{\mathbf{r}}\int \frac{d^3q}{(2\pi)^3}\ \frac{e^{-i\mathbf{q}\mathbf{r}}}{(\mathbf{q}^2+m_g^2)^2} \\ &= \frac{i}{4\pi^2}\nabla_{\mathbf{r}}\int_0^\infty dq\ q^2\int_{-1}^1 d\cos\theta\ \frac{e^{-iqr\cos\theta}}{(q^2+m_g^2)^2} \\ &= \frac{i}{2\pi^2}\nabla_{\mathbf{r}}\left[\frac{1}{r}\int_0^\infty dq\ \frac{q\sin(qr)}{(q^2+m_g^2)^2}\right] = \frac{i}{2\pi^2}\nabla_{\mathbf{r}}\left[r\int_0^\infty dq\ \frac{q\sin q}{(q^2+m_g^2r^2)^2}\right] \\ &= \frac{i}{2\pi^2}\nabla_{\mathbf{r}}\left[\frac{\pi e^{-m_g r}}{4m_g}\right] = -\frac{i\,e^{-m_g r}}{8\pi}\,\hat{\mathbf{r}}\,.\end{aligned} \tag{B.2}$$

In the following, we consider capture into the ground state only, $\{n\ell m\} = \{100\}$.

Following refs. [9, 16, 57], we compute the overlap integrals (B.1) using the identity [72]

$$\int d^3r\ \frac{e^{i(\mathbf{k}-\mathbf{b})\cdot\mathbf{r}-\kappa r}}{4\pi r}\ {}_1F_1[i\zeta_S, 1, i(kr-\mathbf{k}\cdot\mathbf{r})] = \frac{[\mathbf{b}^2+(\kappa-ik)^2]^{-i\zeta_S}}{[(\mathbf{k}-\mathbf{b})^2+\kappa^2]^{1-i\zeta_S}} \equiv f_{\mathbf{k},\mathbf{b}}(\kappa)\,. \tag{B.3}$$

Equations (B.1) become

$$\boldsymbol{\mathcal{J}}_{\mathbf{k},\{100\}}(\mathbf{b}) = \kappa\sqrt{16\pi\kappa^3\,S_0(\zeta_S)}\ [\nabla_{\mathbf{b}} f_{\mathbf{k},\mathbf{b}}(\kappa)]\,, \tag{B.4a}$$

$$\boldsymbol{\mathcal{Y}}_{\mathbf{k},\{100\}} = \mu\alpha_s^{\rm NA}\sqrt{16\pi\kappa^3\,S_0(\zeta_S)}\ [\nabla_{\mathbf{b}} f_{\mathbf{k},\mathbf{b}}(\kappa)]_{\mathbf{b}=0}\,, \tag{B.4b}$$

JHEP07(2018)096

where

$$[\nabla_{\mathbf{b}} f_{\mathbf{k},\mathbf{b}}(\kappa)]_{\mathbf{b}=\mathbf{0}} = \hat{\mathbf{k}}\, \frac{2(1-i\,\zeta_S)}{k^3}\, \frac{\exp\left[-2\zeta_S \operatorname{arccot}(\zeta_B)\right]}{(1+\zeta_B^2)^2}\,. \tag{B.4c}$$

For the cross-sections of interest, we only need $\boldsymbol{\mathcal{J}}_{\mathbf{k},\{100\}}(\mathbf{b})$ evaluated at $\mathbf{b} = \mathbf{0}$ [9, 57]. Evidently,

$$\frac{\boldsymbol{\mathcal{Y}}_{\mathbf{k},\{100\}}}{\boldsymbol{\mathcal{J}}_{\mathbf{k},\{100\}}(\mathbf{0})} = \frac{\alpha_s^{\mathrm{NA}}}{\alpha_g^B}\,, \tag{B.4d}$$

and

$$|\boldsymbol{\mathcal{J}}_{\mathbf{k},\{100\}}(\mathbf{0})|^2 = \frac{2^6\pi}{k}\, S_0(\zeta_S)\,(1+\zeta_S^2)\, \frac{\zeta_B^5\, \exp[-4\zeta_S \operatorname{arccot}(\zeta_B)]}{(1+\zeta_B^2)^4}\,. \tag{B.4e}$$

We recall that ζ_S and ζ_B are defined in eqs. (A.6). In section 2.5, we use eqs. (B.4) to obtain analytical expressions for the BSF cross-sections.

C The non-relativistic Hamiltonian from effective field theory

Our results in section 2 differ from previous computations [55, 56] in the relative sign of the Abelian and non-Abelian contributions to the radiative transition amplitude. In this appendix, we use the non-relativistic QCD (NRQCD) approach of refs. [47, 73, 74] to derive the effective Hamiltonian for our system, and compare it with refs. [55, 56], whose computations are based on effective field theory. This offers an independent check of our computations.

Before moving to NRQCD, we want to display that the discrepancy between our computations and ref. [55] originates from the expression for the transition amplitude. Indeed, starting from eq. (2.25) with $\eta_1 = \eta_2 = 1/2$, and using the coordinate-space expressions for the overlap integrals (B.1) where we integrate eq. (B.1a) by parts, we arrive at

$$\begin{aligned} i[\mathcal{M}_{\mathbf{k}\to\{n\ell m\}}]_{ii',jj'} &= -i[\boldsymbol{\mathcal{M}}_{\mathbf{k}\to\{n\ell m\}}]^a_{ii',jj'}\cdot\boldsymbol{\epsilon}^a \\ &= \sqrt{2^8\pi\alpha_s^{\mathrm{BSF}}\, m_X}\times\left\{\frac{1}{2}\left[(T_1^a)_{i'i}\,\delta_{j'j} - \delta_{i'i}\,(T_2^a)_{j'j}\right]\int d^3r\;[\psi^*_{n\ell m}(\mathbf{r})]\,\nabla\phi_{\mathbf{k}}(\mathbf{r})\right. \\ &\quad \left. - if^{abc}(T_1^b)_{i'i}(T_2^c)_{j'j}\;\frac{m_X\alpha_s^{\mathrm{NA}}}{2}\int d^3r\,\psi^*_{n\ell m}(\mathbf{r})\,\phi_{\mathbf{k}}(\mathbf{r})\,\hat{\mathbf{r}}\right\}\cdot\boldsymbol{\epsilon}^a\,, \end{aligned} \tag{C.1}$$

where $\boldsymbol{\epsilon}^a$ is the gluon polarisation vector. Equation (C.1) may be directly compared to eqs. (41)–(43) of ref. [55]. We observe that the relative sign between the two terms is different.

This discrepancy arises from the non-relativistic Hamiltonian assumed in ref. [55]. The interactions that give rise to the radiative BSF amplitude correspond to a non-relativistic potential $\tilde{V}_{\mathrm{BSF}}(\mathbf{q},\mathbf{p})$ that can be deduced from the transition amplitude $\langle\mathbf{p}|i\mathcal{T}|\mathbf{q}\rangle$ in ordinary quantum mechanics,

$$\langle\mathbf{p}|i\mathcal{T}|\mathbf{q}\rangle = -i\tilde{V}_{\mathrm{BSF}}(\mathbf{q},\mathbf{p})\,, \tag{C.2}$$

where $|\mathbf{q}\rangle$ denotes a state where the two interacting particles have momentum $\mathbf{q}$ and $-\mathbf{q}$ in the CM frame. The quantum mechanical transition amplitude is related to the matrix element $\mathcal{M}(\mathbf{q},\mathbf{p}) = -\boldsymbol{\mathcal{M}}^a_{\mathrm{trans}}(\mathbf{q},\mathbf{p})\cdot\boldsymbol{\epsilon}^a$ via

$$(4m_X^2/A_0)\;\langle\mathbf{p}|i\mathcal{T}|\mathbf{q}\rangle = -i\boldsymbol{\mathcal{M}}^a_{\mathrm{trans}}(\mathbf{q},\mathbf{p})\cdot\boldsymbol{\epsilon}^a\;(2\pi)\delta(E_{\mathbf{q}} - E_{\mathbf{p}} - \omega)\,, \tag{C.3}$$

where the factor $4m_X^2/A_0$ accounts for the different normalization of fields in quantum field theory and quantum mechanics, with A_0 being the non-relativistic normalisation of the gauge field. $E_{\mathbf{q}}$, $E_{\mathbf{p}}$ are the energies of the $|\mathbf{q}\rangle$, $|\mathbf{p}\rangle$ states and ω is the energy of the radiated gauge boson. From eqs. (C.2) and (C.3), we identify the non-relativistic potential in momentum space as

$$\tilde{V}_{\rm BSF}(\mathbf{q},\mathbf{p}) = \left(\frac{A_0}{4m_X^2}\right) \boldsymbol{\mathcal{M}}^a_{\rm trans}(\mathbf{q},\mathbf{p})\cdot\boldsymbol{\epsilon}^a\ (2\pi)\delta(E_{\mathbf{q}}-E_{\mathbf{p}}-\omega)\,. \tag{C.4}$$

The potential in coordinate space is[8]

$$V_{\rm BSF}(t,\mathbf{r}) = \int \frac{d(E_{\mathbf{q}}-E_{\mathbf{p}})}{(2\pi)}\frac{d^3(\mathbf{q}-\mathbf{p})}{(2\pi)^3}\ e^{i[(E_{\mathbf{q}}-E_{\mathbf{p}})\cdot t-(\mathbf{q}-\mathbf{p})\cdot\mathbf{r}]}\ \tilde{V}_{\rm BSF}(\mathbf{q},\mathbf{p})\,. \tag{C.5}$$

Using eq. (2.24) for $\boldsymbol{\mathcal{M}}^a_{\rm trans}(\mathbf{q},\mathbf{p})$ and the identity (B.2), we obtain

$$\begin{aligned} V_{\rm BSF}(t,\mathbf{r}) = -A_0\boldsymbol{\epsilon}^a\cdot\Bigg\{ &\frac{g_s^{\rm BSF}}{m_X}\left[(T_1^a)_{i'i}\,\delta_{j'j}e^{i(\omega t-\mathbf{P}_g\cdot\mathbf{r}/2)} - \delta_{i'i}\,(T_2^a)_{j'j}e^{i(\omega t+\mathbf{P}_g\cdot\mathbf{r}/2)}\right]\mathbf{q} \\ &-g_s^{\rm BSF}\alpha_s^{\rm NA}f^{abc}(T_1^b)_{i'i}(T_2^c)_{j'j}\,e^{i\omega t}\ \hat{\mathbf{r}}\Bigg\}\,. \end{aligned} \tag{C.6}$$

Identifying $\mathbf{A}^a(t,\mathbf{x}) = A_0\exp[i(\omega t-\mathbf{P}_g\cdot\mathbf{x})]\,\boldsymbol{\epsilon}^a$ as the background field that induces the transition (see e.g. [75, section 5.7]), we rewrite the above as follows

$$\begin{aligned} V_{\rm BSF}(t,\mathbf{r}) = -\Bigg\{ &\frac{g_s^{\rm BSF}}{m_X}\left[(T_1^a)_{i'i}\,\delta_{j'j}\,\mathbf{q}\cdot\mathbf{A}^a(t,\mathbf{r}/2) - \delta_{i'i}\,(T_2^a)_{j'j}\,\mathbf{q}\cdot\mathbf{A}^a(t,-\mathbf{r}/2)\right] \\ &-g_s^{\rm BSF}\alpha_s^{\rm NA}f^{abc}(T_1^b)_{i'i}(T_2^c)_{j'j}\ \hat{\mathbf{r}}\cdot\mathbf{A}^a(t,\mathbf{0})\Bigg\}\,. \end{aligned} \tag{C.7}$$

Comparing this with eq. (36) of ref. [55], we note the difference in the relative sign of the Abelian and non-Abelian contributions.

We now move on to NRQCD. At leading order, a heavy quark-antiquark system yields the same potential as a scalar particle-antiparticle system. Thus, we may compare our result of eq. (C.7) with that derived for quarkonium in NRQCD, where the "potential" gluons are integrated out, leaving four-quark operators in the effective Lagrangian in analogy to the Fermi theory. There are different formulations, e.g. pNRQCD [47, 76] or vNRQCD [73, 74, 77].[9] Here, we will follow the conventions of [73, 74, 79]. We start from the ultrasoft NRQCD Lagrangian given in eq. (7) of ref. [73]

$$\mathcal{L}_u \supset \sum_{\mathbf{p}}\psi^\dagger_{\mathbf{p}}\left\{iD^0 - \frac{(\mathbf{p}-i\mathbf{D})^2}{2m} + \frac{\mathbf{p}^4}{8m^3}\right\}\psi_{\mathbf{p}} + \sum_{\mathbf{p}}\chi^\dagger_{\mathbf{p}}\left\{iD^0 - \frac{(\mathbf{p}-i\mathbf{D})^2}{2m} + \frac{\mathbf{p}^4}{8m^3}\right\}\chi_{\mathbf{p}}\,, \tag{C.8}$$

where $D^\mu = \partial^\mu + ig_sA^{a\mu}T^a = (D^0,-\mathbf{D})$ with $D^0 = \partial^0 + ig_sA^{a0}T^a$ and $\mathbf{D} = \nabla - ig_s\mathbf{A}^aT^a$. The momentum $\mathbf{p}$ represents momenta of the soft scale. In contrast to the usual relativistic

[8] Note that we Fourier transform only with respect to the energy and momentum differences between the initial and final X_1X_2 states, thus the coordinate-space potential may still depend on $\mathbf{q}$ [cf. eq. (C.7)].

[9] For a comprehensive comparison, we refer to [78].

JHEP07(2018)096

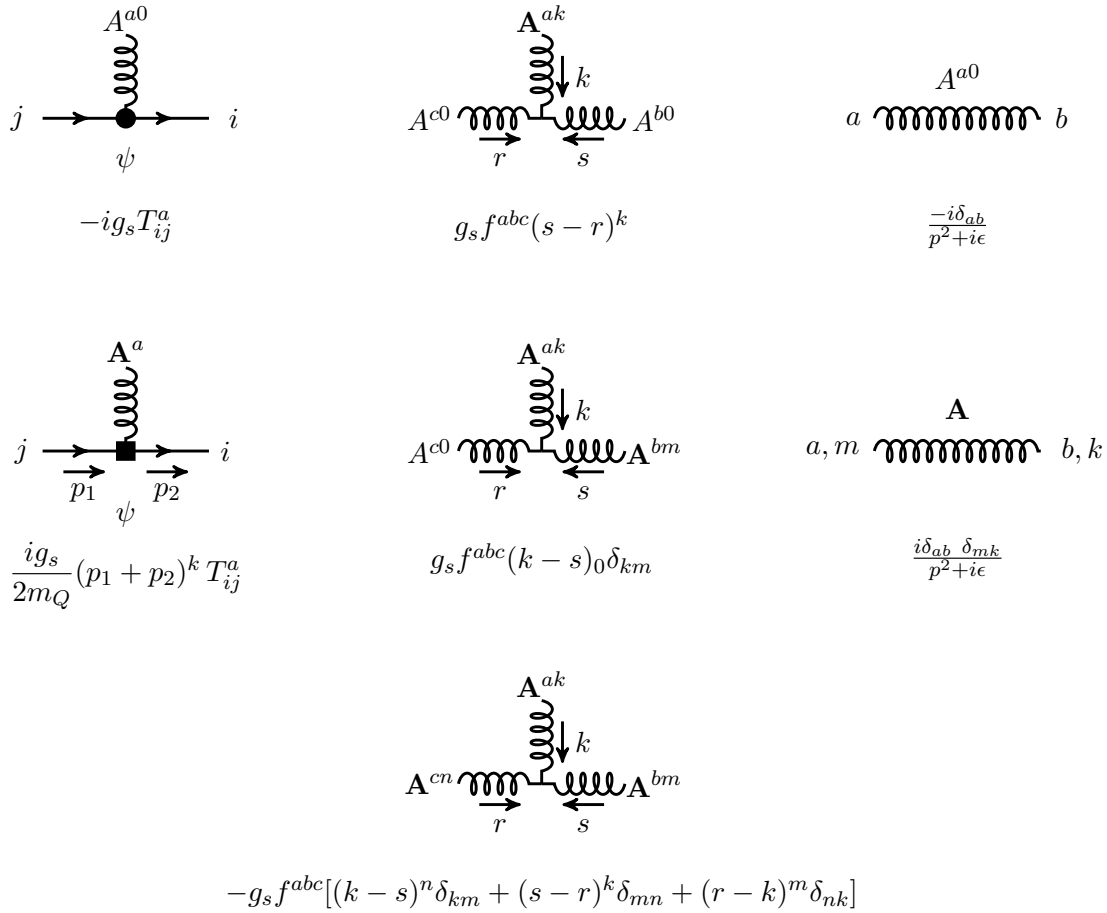

Figure 8. Feynman rules that are used to derive the non-relativistic potential that determines the radiative capture into bound states. In the gauge fields $A^{a,\mu}$, the first index denotes colour, while the second one if the space-time index. The first column depicts the NRQCD Feynman rules which distinguish between temporal (black dot) and spatial (black rectangle) couplings in the quark-gluon vertex. Hereby, ψ represents a fermion field. The Feynman rules for the anti-fermion field χ are obtained by simply substituting $T^a_{ij} \to \overline{T}^a_{ij} = -T^a_{ji}$. The second column shows the non-relativistic 3-gluon-vertex, and the third column shows the gluon propagators. We distinguish again between temporal and spatial gauge fields. Note that according to the NRQCD Lagrangian (C.8), the NRQCD Feynman rules are defined with upper indices only, and incorporate the signs arising from the metric, $g_{\mu\nu} = \mathrm{diag}(1,-1,-1,-1)$, in 4-vector contractions done according to the relativistic conventions.

conventions, here $\psi^\dagger$ ($\chi^\dagger$) annihilates (anti)particles, while ψ (χ) creates (anti)particles. Their generators are related via $\overline{T}^a_{ij} = -T^a_{ji}$. m_Q denotes the (anti)quark mass. From eq. (C.8), we can derive the Feynman rules for the fermion-antifermion system, treating the temporal and spatial component of the gauge field separately. We present them in figure 8.

We may now compute the contributions to the radiative transition amplitudes, shown in figure 9. In the CM frame, the momenta of the incoming/outgoing fermions are

$$q_1^\mu = (q_1^0,\ \mathbf{q})\,, \qquad q_2^\mu = (q_2^0,\ -\mathbf{q})\,, \tag{C.9a}$$

$$p_1^\mu = (p_1^0,\ -\mathbf{P}_g/2 + \mathbf{p})\,, \qquad p_2^\mu = (p_2^0,\ -\mathbf{P}_g/2 - \mathbf{p})\,, \tag{C.9b}$$

JHEP07(2018)096

where $\mathbf{P}_g$ is the momentum of the emitted gluon. The energies of the scattering and bound states are

$$(q_1+q_2)^0 = 2m_Q + \mathbf{k}^2/m_Q\,, \tag{C.9c}$$

$$(p_1+p_2)^0 = M_B + \mathbf{P}_g^2/(2M_B)\,, \tag{C.9d}$$

where $\mathbf{k}$ is the expectation value of $\mathbf{q}$ and $M_B = 2m_Q - E_B$ is the mass of the bound state, with E_B being the binding energy (cf. appendix A). The energy of the radiated gluon, $\omega = |\mathbf{P}_g|$, is found from the conservation of energy to be [cf. eq. (2.20)],

$$\omega = (q_1+q_2-p_1-p_2)^0 \simeq E_B + \mathbf{k}^2/m_Q\,. \tag{C.10}$$

In the following, we shall extract the leading order contributions to the radiative BSF amplitude taking into account that $|\mathbf{q}| \sim |\mathbf{k}| = (m_Q/2)v_{\rm rel}$, $|\mathbf{p}| \sim \kappa = (m_Q/2)\alpha_s$ and $\omega = (m_Q/4)(\alpha_s^2 + v_{\rm rel}^2)$.

From the Lagrangian of eq. (C.8) and the Feynman rules of figure 8, it is straightforward to obtain the Abelian contributions to the transition amplitude, shown in figure 9a,

$$\begin{aligned} i\mathcal{W}_{\rm Abelian} &= \\ &= \frac{ig_s}{2m_Q}\left[(\mathbf{q}_1+\mathbf{p}_1)T^a_{i'i}\delta_{jj'}(2\pi)^3\delta^3(\mathbf{q}_1-\mathbf{p}_1-\mathbf{P}_g)+(\mathbf{q}_2+\mathbf{p}_2)\overline{T}^a_{j'j}\delta_{ii'}(2\pi)^3\delta^3(\mathbf{q}_2-\mathbf{p}_2-\mathbf{P}_g)\right]\boldsymbol{\epsilon}^a \\ &\simeq \frac{ig_s}{m_Q}\left[T^a_{i'i}\delta_{jj'}\,(2\pi)^3\delta^3(\mathbf{q}-\mathbf{p}-\mathbf{P}_g/2)-\overline{T}^a_{j'j}\delta_{i'i}\,(2\pi)^3\delta^3(\mathbf{q}-\mathbf{p}+\mathbf{P}_g/2)\right](\mathbf{q}\cdot\boldsymbol{\epsilon}^a)\,. \end{aligned} \tag{C.11}$$

We shall now derive the potential NRQCD Lagrangian term that describes the non-Abelian contribution to the radiative transition amplitudes. We will demonstrate that (a) we recover the same sign as in [73, 74, 79] using our conventions eqs. (C.2) and (C.3), and that (b) this sign disagrees with the result of [55]. From the NRQCD Feynman rules of figure 8, it is immediately evident that the first of the four diagrams shown in figure 9b yields the dominant contribution (see also comment below eqs. (2.23)). The diagrams involving the spatial components of the gluon propagators are suppressed by higher orders in the momenta $\mathbf{q}$ and $\mathbf{p}$, as shown explicitly below. Allowing for a non-zero gluon mass m_g, we obtain the following contributions for $i\mathcal{W}_{\rm NA}$ respectively:

$$\begin{aligned} i\mathcal{W}_{\bullet\bullet} &= (-ig_sT^b_{i'i})(-ig_s\overline{T}^c_{j'j})\left[\frac{-i}{(q_1-p_1)^2-m_g^2}\right]\left[\frac{-i}{(q_2-p_2)^2-m_g^2}\right] \\ &\quad\times g_sf^{abc}(q_1-p_1-q_2+p_2)^k\epsilon^{a,k} \\ &\simeq\; 2g_s^2g_s\; f^{abc}T^b_{i'i}\overline{T}^c_{j'j}\;\frac{(\mathbf{q}-\mathbf{p})}{[(\mathbf{q}-\mathbf{p})^2+m_g^2]^2}\cdot\boldsymbol{\epsilon}^a\,, \end{aligned} \tag{C.12a}$$

$$\begin{aligned} i\mathcal{W}_{\blacksquare\blacksquare} &= \left[\frac{ig_s}{2m_Q}(q_1+p_1)^m\,T^b_{i'i}\right]\left[\frac{ig_s}{2m_Q}(q_2+p_2)^n\,\overline{T}^c_{j'j}\right]\left[\frac{i\delta_{mm'}}{(q_1-p_1)^2-m_g^2}\right]\left[\frac{i\delta_{nn'}}{(q_2-p_2)^2-m_g^2}\right] \\ &\quad\times(-g_s)f^{abc}\,\epsilon^{a,k} \\ &\quad\times\left[(q_1-p_1-q_2+p_2)^k\delta_{m'n'}+(q_2-p_2+P_g)^{m'}\delta_{n'k}+(-P_g-q_1+p_1)^{n'}\delta_{km'}\right] \\ &\simeq g_s^2g_sf^{abc}T^b_{i'i}\overline{T}^c_{j'j}\;\frac{[(\mathbf{q}+\mathbf{p})^2(\mathbf{q}-\mathbf{p})+(\mathbf{p}^2-\mathbf{q}^2)(\mathbf{q}+\mathbf{p})]}{2m_Q^2\,[(\mathbf{q}-\mathbf{p})^2+m_g^2]^2}\cdot\boldsymbol{\epsilon}^a\,, \end{aligned} \tag{C.12b}$$

JHEP07(2018)096

$$
\begin{aligned}
i\mathcal{W}_{\bullet\blacksquare} &= \left[\frac{ig_s}{2m_Q}T^b_{i'i}(q_1+p_1)^m\right](-ig_s\overline{T}^c_{j'j})\left[\frac{i\delta_{mm'}}{(q_1-p_1)^2-m_g^2}\right]\left[\frac{-i}{(q_2-p_2)^2-m_g^2}\right] \\
&\quad\times g_s f^{abc}(-P_g-q_1+p_1)^0\delta_{km'}\,\epsilon^{a,k} \\
&\simeq -g_s^2 g_s f^{abc}T^b_{i'i}\overline{T}^c_{j'j}\left[\frac{(q_1-p_1+P_g)^0}{2m_Q}\right]\frac{(\mathbf{q}+\mathbf{p})}{[(\mathbf{q}-\mathbf{p})^2+m_g^2]^2}\cdot\boldsymbol{\epsilon}^a\,, \qquad \text{(C.12c)} \\
i\mathcal{W}_{\blacksquare\bullet} &= (-ig_sT^b_{i'i})\left[\frac{ig_s}{2m_Q}\overline{T}^c_{j'j}(q_2+p_2)^n\right]\left[\frac{-i}{(q_1-p_1)^2-m_g^2}\right]\left[\frac{i\delta_{nn'}}{(q_2-p_2)^2-m_g^2}\right] \\
&\quad\times g_s f^{abc}(q_2-p_2+P_g)^0\delta_{n'k}\,\epsilon^{a,k} \\
&\simeq -g_s^2 g_s f^{abc}T^b_{i'i}\overline{T}^c_{j'j}\left[\frac{(q_2-p_2+P_g)^0}{2m_Q}\right]\frac{(\mathbf{q}+\mathbf{p})}{[(\mathbf{q}-\mathbf{p})^2+m_g^2]^2}\cdot\boldsymbol{\epsilon}^a\,,
\end{aligned}
$$

where we have used eqs. (C.9). Using the energy conservation (C.10), the last two terms add up to

$$
i(\mathcal{W}_{\bullet\blacksquare}+\mathcal{W}_{\blacksquare\bullet}) \simeq -g_s^2 g_s f^{abc}T^b_{i'i}\overline{T}^c_{j'j}\left(\frac{3\omega}{2m_Q}\right)\frac{(\mathbf{q}+\mathbf{p})}{[(\mathbf{q}-\mathbf{p})^2+m_g^2]^2}\cdot\boldsymbol{\epsilon}^a\,. \qquad \text{(C.12d)}
$$

Since $|\mathbf{q}|^2$, $|\mathbf{p}|^2$, $\omega \ll m_Q$, the terms $\mathcal{W}_{\blacksquare\blacksquare}$, $\mathcal{W}_{\blacksquare\bullet}$ and $\mathcal{W}_{\bullet\blacksquare}$ are subdominant with respect to $\mathcal{W}_{\bullet\bullet}$. Thus, the leading order non-Abelian contribution is $\mathcal{W}_{\rm NA} \simeq \mathcal{W}_{\bullet\bullet}$, which agrees with our findings in section 2.3.

The total transition amplitude is $i\mathcal{W}_{\rm trans} \simeq i\mathcal{W}_{\rm Abelian} + i\mathcal{W}_{\rm NA}$. Collecting eqs. (C.11) and (C.12a), we find it to be

$$
\begin{aligned}
i\mathcal{W}_{\rm trans} \simeq \frac{i2g_s}{m_Q}\Bigg\{&\left[\frac{1}{2}T^a_{i'i}\delta_{jj'}\,(2\pi)^3\delta^3(\mathbf{q}-\mathbf{p}-\mathbf{P}_g/2)-\frac{1}{2}\overline{T}^a_{j'j}\delta_{i'i}\,(2\pi)^3\delta^3(\mathbf{q}-\mathbf{p}+\mathbf{P}_g/2)\right]\mathbf{q} \\
&-i8\pi f^{abc}T^b_{i'i}\overline{T}^c_{j'j}\left(\frac{m_Q\alpha_s}{2}\right)\frac{(\mathbf{q}-\mathbf{p})}{[(\mathbf{q}-\mathbf{p})^2+m_g^2]^2}\Bigg\}\cdot\boldsymbol{\epsilon}^a\,. \qquad \text{(C.13)}
\end{aligned}
$$

This can be compared with $i\mathcal{M}_{\rm trans}/(4M\mu) = -i\boldsymbol{\mathcal{M}}^a_{\rm trans}\cdot\boldsymbol{\epsilon}^a/(4M\mu)$ with $\boldsymbol{\mathcal{M}}_{\rm trans}$ given by eq. (2.24). As earlier, the factor $4M\mu$ accounts for the relativistic normalisation of states. We see that the two results are in agreement.

In order to compare eq. (C.13) with [73, 79], we construct the effective action that recovers the amplitude,

$$
\langle p_1,p_2|iS_{\rm eff}|q_1,q_2\rangle = (2\pi)^4\delta^{(4)}(q_1+q_2-p_1-p_2)\,i\mathcal{W}_{\rm trans}(q_1,q_2,p_1,p_2)\,, \qquad \text{(C.14)}
$$

such that

$$
\begin{aligned}
S_{\rm eff} = \int\frac{d^4q_1d^4q_2d^4p_1d^4p_2}{(2\pi)^{16}}\,&\psi^\dagger(p_1)\chi^\dagger(p_2)\,\mathcal{W}_{\rm trans}(q_1,q_2,p_1,p_2)\,\psi(q_1)\chi(q_2) \\
&\times(2\pi)^4\delta^{(4)}(q_1+q_2-p_1-p_2)\,. \qquad \text{(C.15)}
\end{aligned}
$$

Exchanging the polarisation vector $\boldsymbol{\epsilon}^a$ for the background field $\mathbf{A}^a$, we arrive at the Lagrangian

$$
\begin{aligned}
\mathcal{L}_u+\mathcal{L}_p \supset &\sum_{\mathbf{p}}\psi^\dagger_{\mathbf{p}}\left\{iD^0-\frac{(\mathbf{p}-i\mathbf{D})^2}{2m}+\frac{\mathbf{p}^4}{8m^3}\right\}\psi_{\mathbf{p}}+\sum_{\mathbf{p}}\chi^\dagger_{\mathbf{p}}\left\{iD^0-\frac{(\mathbf{p}-i\mathbf{D})^2}{2m}+\frac{\mathbf{p}^4}{8m^3}\right\}\chi_{\mathbf{p}} \\
&+\sum_{\mathbf{p},\mathbf{q}}(-2ig_s^2g_s\;f^{abc})\left(\psi^\dagger_{\mathbf{p}}T^b\psi_{\mathbf{q}}\right)\left(\chi^\dagger_{-\mathbf{p}}\overline{T}^c\chi_{-\mathbf{q}}\right)\frac{(\mathbf{q}-\mathbf{p})}{(\mathbf{q}-\mathbf{p})^4}\cdot\mathbf{A}^a\,. \qquad \text{(C.16)}
\end{aligned}
$$

JHEP07(2018)096

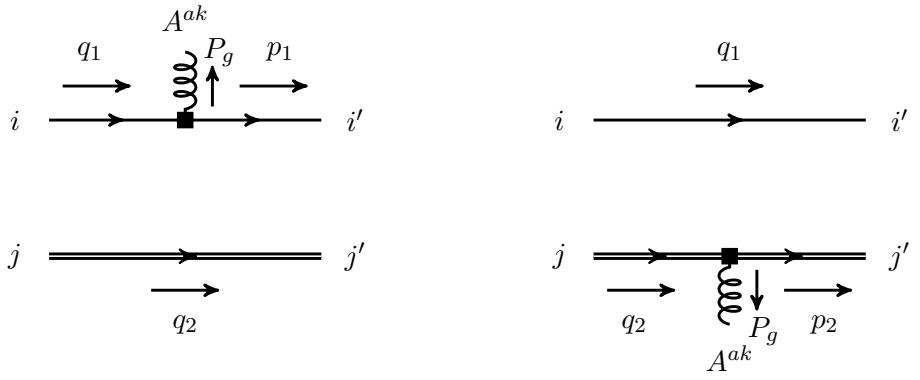

(a) Abelian contributions.

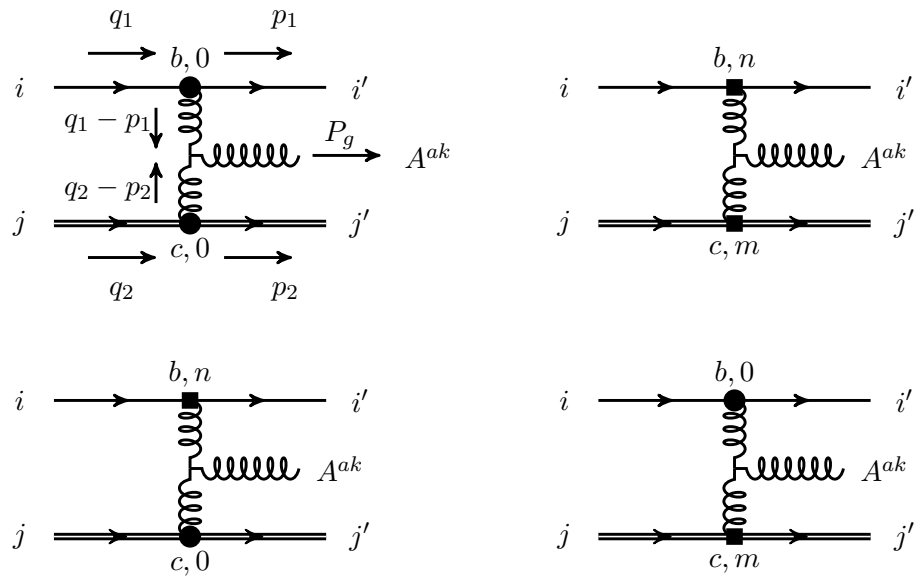

(b) Non-Abelian contributions. As in figure 8, we distinguish between the temporal (circle) and spatial (rectangle) components of $A^{a\mu}$.

Figure 9. Gluon emission diagrams contributing to the radiative capture of a fermion-antifermion pair into a bound state. The fermion field ψ is depicted as a solid line, the antifermion field χ as a double line.

This Lagrangian can be compared with eqs. (6), (7), (12) and the first term of eq. (16) of ref. [73].[10] It agrees perfectly, including the sign of the non-Abelian term.[11]

Similarly to before, we may now derive the full interaction potential in position space. Starting from eq. (C.13) and following similar steps as in the beginning of this appendix, we arrive again at eq. (C.7), with the identification $T^a_{i'i} = (T_1)^a_{i'i}$, $\overline{T}^a_{j'j} = (T_2)^a_{j'j} = -(T_1)^a_{jj'}$ and $m_Q = m_X$, thereby confirming the validity of the computation of section 2 and the

[10] Note that $\mathbf{k}$ in eq. (16) of ref. [73] is defined as $\mathbf{k} = -(\mathbf{q} - \mathbf{p})$.

[11] The effective Lagrangian is invariant under ultrasoft gauge transformations [47, 79].

JHEP07(2018)096

disagreement with ref. [55]. We note that we have also compared our results to those of ref. [47] and found them in agreement.[12]

D The Milne relation

For a 2-to-2 process $1+2 \leftrightarrow A+B$, the cross-section, averaged over the degrees of freedom of the initial state, is

$$\sigma_{1+2\to A+B} = \frac{1}{g_1 g_2} \frac{1}{2\sqrt{(s-m_1^2-m_2^2)^2-4m_1^2m_2^2}} \frac{|\mathbf{P}_A^{\rm CM}|}{16\pi^2\sqrt{s}} \int d\Omega \, |\mathcal{M}_{1+2\to A+B}|^2 \,, \quad \text{(D.1)}$$

where s is the first Mandelstam variable and $\mathbf{P}_A^{\rm CM}$ is the momentum of A (or B) in the CM frame. Since $|\mathcal{M}_{1+2\to A+B}|^2 = |\mathcal{M}_{A+B\to 1+2}|^2$, the cross-sections of two 2-to-2 inverse processes are related via

$$\frac{\sigma_{A+B\to 1+2}}{\sigma_{1+2\to A+B}} = \frac{g_1 g_2}{g_A g_B} \left[\frac{(s-m_1^2-m_2^2)^2-4m_1^2m_2^2}{(s-m_A^2-m_B^2)^2-4m_A^2m_B^2}\right]^{1/2} \frac{|\mathbf{P}_1|}{|\mathbf{P}_A|} \,. \quad \text{(D.2)}$$

We now consider the radiative BSF and ionisation processes $X_1 + X_2 \leftrightarrow \mathcal{B}_{n\ell} + g$, where g stands generally for the massless field radiated in a BSF process with energy ω. In the non-relativistic regime,

$$s \simeq (m_1 + m_2 + \mathcal{E}_{\mathbf{k}})^2 \simeq (m_1 + m_2 + \mathcal{E}_{n\ell} + \omega)^2 \,, \quad \text{(D.3)}$$

where $\mathcal{E}_{\mathbf{k}} = \mu v_{\rm rel}^2/2$ is the kinetic energy of the initial state in the CM frame, and $\mathcal{E}_{n\ell} < 0$ is the binding energy of the bound state (cf. appendix A), with $\mathcal{E}_{\mathbf{k}}$, $|\mathcal{E}_{n\ell}| \ll m_1 + m_2$. Then, $|\mathbf{P}_1| = |\mathbf{P}_2| = \mu v_{\rm rel}$ and $|\mathbf{P}_g| = |\mathbf{P}_{\mathcal{B}}| = \omega = \mathcal{E}_{\mathbf{k}} - \mathcal{E}_{n\ell}$, and from eq. (D.2) we find the Milne relation

$$\sigma_{\rm ion} = \frac{g_1 g_2}{g_g g_{\mathcal{B}}} \left(\frac{\mu^2 v_{\rm rel}^2}{\omega^2}\right) \sigma_{\rm BSF} \,. \quad \text{(D.4)}$$

Acknowledgments

We thank Adam Falkowski, Carlos Tamarit and Simone Biondini for useful discussions. J.H. was supported by the Labex ILP (reference ANR-10-LABX-63) part of the Idex SUPER, and received financial state aid managed by the Agence Nationale de la Recherche, as part of the programme Investissements d'avenir under the reference ANR-11-IDEX-0004-02. K.P. was supported by the ANR ACHN 2015 grant ("TheIntricateDark" project), and by the NWO Vidi grant "Self-interacting asymmetric dark matter".

[12] For comparison with eq. (1.8) in ref. [47], it is important to note the different definition of fields with respect to ref. [73]. In ref. [47], ψ ($\chi^\dagger$) annihilates (anti)particles, while $\psi^\dagger$ (χ) creates (anti)particles. In that notation, one has to account for the odd Wick permutations, such that the corresponding non-Abelian amplitude $\mathcal{M}'_{\rm NA}$ is recovered by

$$S_{\rm eff} = \int \frac{d^4q_1 d^4q_2 d^4p_1 d^4p_2}{(2\pi)^{16}} \psi^\dagger(p_1)\chi(-p_2)\,(-1)\,\mathcal{M}'_{\rm NA}(q_1,q_2,p_1,p_2)\psi(q_1)\chi^\dagger(-q_2) \,, \quad \text{(C.17)}$$

in contrast to eq. (C.15). From $\mathcal{M}'_{\rm NA}$, we may derive the non-relativistic potential, as in the beginning of this appendix, and compare it with eq. (C.7). A global sign difference is expected due to the different definition for the covariant derivative: while here we have used $D_\mu = \partial_\mu + ig_s A_\mu^a T^a$, in ref. [47] the covariant derivative is defined as $D_\mu = \partial_\mu - ig_s A_\mu^a T^a$.

JHEP07(2018)096

References

[1] M. Pospelov and A. Ritz, *Astrophysical Signatures of Secluded Dark Matter*, *Phys. Lett.* **B 671** (2009) 391 [arXiv:0810.1502] [INSPIRE].

[2] J.D. March-Russell and S.M. West, *WIMPonium and Boost Factors for Indirect Dark Matter Detection*, *Phys. Lett.* **B 676** (2009) 133 [arXiv:0812.0559] [INSPIRE].

[3] W. Shepherd, T.M.P. Tait and G. Zaharijas, *Bound states of weakly interacting dark matter*, *Phys. Rev.* **D 79** (2009) 055022 [arXiv:0901.2125] [INSPIRE].

[4] B. von Harling and K. Petraki, *Bound-state formation for thermal relic dark matter and unitarity*, *JCAP* **12** (2014) 033 [arXiv:1407.7874] [INSPIRE].

[5] I. Baldes and K. Petraki, *Asymmetric thermal-relic dark matter: Sommerfeld-enhanced freeze-out, annihilation signals and unitarity bounds*, *JCAP* **09** (2017) 028 [arXiv:1703.00478] [INSPIRE].

[6] H. An, M.B. Wise and Y. Zhang, *Effects of Bound States on Dark Matter Annihilation*, *Phys. Rev.* **D 93** (2016) 115020 [arXiv:1604.01776] [INSPIRE].

[7] H. An, M.B. Wise and Y. Zhang, *Strong CMB Constraint On P-Wave Annihilating Dark Matter*, *Phys. Lett.* **B 773** (2017) 121 [arXiv:1606.02305] [INSPIRE].

[8] P. Asadi, M. Baumgart, P.J. Fitzpatrick, E. Krupczak and T.R. Slatyer, *Capture and Decay of Electroweak WIMPonium*, *JCAP* **02** (2017) 005 [arXiv:1610.07617] [INSPIRE].

[9] K. Petraki, M. Postma and J. de Vries, *Radiative bound-state-formation cross-sections for dark matter interacting via a Yukawa potential*, *JHEP* **04** (2017) 077 [arXiv:1611.01394] [INSPIRE].

[10] M. Cirelli, P. Panci, K. Petraki, F. Sala and M. Taoso, *Dark Matter's secret liaisons: phenomenology of a dark* U(1) *sector with bound states*, *JCAP* **05** (2017) 036 [arXiv:1612.07295] [INSPIRE].

[11] C. Kouvaris, K. Langæble and N.G. Nielsen, *The Spectrum of Darkonium in the Sun*, *JCAP* **10** (2016) 012 [arXiv:1607.00374] [INSPIRE].

[12] I. Baldes, M. Cirelli, P. Panci, K. Petraki, F. Sala and M. Taoso, *Asymmetric dark matter: residual annihilations and self-interactions*, *SciPost Phys.* **4** (2018) 041 [arXiv:1712.07489] [INSPIRE].

[13] K. Petraki and R.R. Volkas, *Review of asymmetric dark matter*, *Int. J. Mod. Phys.* **A 28** (2013) 1330028 [arXiv:1305.4939] [INSPIRE].

[14] R. Laha and E. Braaten, *Direct detection of dark matter in universal bound states*, *Phys. Rev.* **D 89** (2014) 103510 [arXiv:1311.6386] [INSPIRE].

[15] A. Butcher, R. Kirk, J. Monroe and S.M. West, *Can Tonne-Scale Direct Detection Experiments Discover Nuclear Dark Matter?*, *JCAP* **10** (2017) 035 [arXiv:1610.01840] [INSPIRE].

[16] L. Pearce and A. Kusenko, *Indirect Detection of Self-Interacting Asymmetric Dark Matter*, *Phys. Rev.* **D 87** (2013) 123531 [arXiv:1303.7294] [INSPIRE].

JHEP07(2018)096

[17] J.M. Cline, Y. Farzan, Z. Liu, G.D. Moore and W. Xue, *3.5 keV x rays as the "21 cm line" of dark atoms and a link to light sterile neutrinos*, *Phys. Rev.* **D 89** (2014) 121302 [arXiv:1404.3729] [INSPIRE].

[18] W. Detmold, M. McCullough and A. Pochinsky, *Dark Nuclei I: Cosmology and Indirect Detection*, *Phys. Rev.* **D 90** (2014) 115013 [arXiv:1406.2276] [INSPIRE].

[19] L. Pearce, K. Petraki and A. Kusenko, *Signals from dark atom formation in halos*, *Phys. Rev.* **D 91** (2015) 083532 [arXiv:1502.01755] [INSPIRE].

[20] K. Petraki, L. Pearce and A. Kusenko, *Self-interacting asymmetric dark matter coupled to a light massive dark photon*, *JCAP* **07** (2014) 039 [arXiv:1403.1077] [INSPIRE].

[21] S.J. Lonsdale and R.R. Volkas, *Grand unified hidden-sector dark matter*, *Phys. Rev.* **D 90** (2014) 083501 [*Erratum ibid.* **D 91** (2015) 129906] [arXiv:1407.4192] [INSPIRE].

[22] S.J. Lonsdale, M. Schroor and R.R. Volkas, *Asymmetric Dark Matter and the hadronic spectra of hidden QCD*, *Phys. Rev.* **D 96** (2017) 055027 [arXiv:1704.05213] [INSPIRE].

[23] S.J. Lonsdale and R.R. Volkas, *Comprehensive asymmetric dark matter model*, *Phys. Rev.* **D 97** (2018) 103510 [arXiv:1801.05561] [INSPIRE].

[24] H. An, B. Echenard, M. Pospelov and Y. Zhang, *Probing the Dark Sector with Dark Matter Bound States*, *Phys. Rev. Lett.* **116** (2016) 151801 [arXiv:1510.05020] [INSPIRE].

[25] Z. Kang, *Bound states via Higgs exchanging and heavy resonant di-Higgs*, *Phys. Lett.* **B 771** (2017) 313 [arXiv:1606.01531] [INSPIRE].

[26] G. Elor, H. Liu, T.R. Slatyer and Y. Soreq, *Complementarity for Dark Sector Bound States*, arXiv:1801.07723 [INSPIRE].

[27] S.R. Coleman, *Q Balls*, *Nucl. Phys.* **B 262** (1985) 263 [*Erratum ibid.* **B 269** (1986) 744] [INSPIRE].

[28] A. Kusenko and M.E. Shaposhnikov, *Supersymmetric Q balls as dark matter*, *Phys. Lett.* **B 418** (1998) 46 [hep-ph/9709492] [INSPIRE].

[29] A. Kusenko, *Small Q balls*, *Phys. Lett.* **B 404** (1997) 285 [hep-th/9704073] [INSPIRE].

[30] A. Kusenko, *Solitons in the supersymmetric extensions of the standard model*, *Phys. Lett.* **B 405** (1997) 108 [hep-ph/9704273] [INSPIRE].

[31] A. Kusenko and P.J. Steinhardt, *Q ball candidates for selfinteracting dark matter*, *Phys. Rev. Lett.* **87** (2001) 141301 [astro-ph/0106008] [INSPIRE].

[32] J. Harz, B. Herrmann, M. Klasen, K. Kovarik and Q.L. Boulc'h, *Neutralino-stop coannihilation into electroweak gauge and Higgs bosons at one loop*, *Phys. Rev.* **D 87** (2013) 054031 [arXiv:1212.5241] [INSPIRE].

[33] J. Harz, B. Herrmann, M. Klasen, K. Kovařík and M. Meinecke, *SUSY-QCD corrections to stop annihilation into electroweak final states including Coulomb enhancement effects*, *Phys. Rev.* **D 91** (2015) 034012 [arXiv:1410.8063] [INSPIRE].

[34] J. Harz, B. Herrmann, M. Klasen and K. Kovarik, *One-loop corrections to neutralino-stop coannihilation revisited*, *Phys. Rev.* **D 91** (2015) 034028 [arXiv:1409.2898] [INSPIRE].

[35] M.J. Baker et al., *The Coannihilation Codex*, *JHEP* **12** (2015) 120 [arXiv:1510.03434] [INSPIRE].

[36] A. Ibarra, A. Pierce, N.R. Shah and S. Vogl, *Anatomy of Coannihilation with a Scalar Top Partner*, *Phys. Rev.* **D 91** (2015) 095018 [arXiv:1501.03164] [INSPIRE].

JHEP07(2018)096

[37] J. Harz, B. Herrmann, M. Klasen, K. Kovarik and P. Steppeler, *Theoretical uncertainty of the supersymmetric dark matter relic density from scheme and scale variations*, *Phys. Rev.* **D 93** (2016) 114023 [arXiv:1602.08103] [INSPIRE].

[38] S.P. Liew and F. Luo, *Effects of QCD bound states on dark matter relic abundance*, *JHEP* **02** (2017) 091 [arXiv:1611.08133] [INSPIRE].

[39] A. Pierce, N.R. Shah and S. Vogl, *Stop Co-Annihilation in the Minimal Supersymmetric Standard Model Revisited*, *Phys. Rev.* **D 97** (2018) 023008 [arXiv:1706.01911] [INSPIRE].

[40] H.E. Haber, R. Hempfling and A.H. Hoang, *Approximating the radiatively corrected Higgs mass in the minimal supersymmetric model*, *Z. Phys.* **C 75** (1997) 539 [hep-ph/9609331] [INSPIRE].

[41] H.E. Haber and R. Hempfling, *Can the mass of the lightest Higgs boson of the minimal supersymmetric model be larger than m_Z?*, *Phys. Rev. Lett.* **66** (1991) 1815 [INSPIRE].

[42] A. Hryczuk, I. Cholis, R. Iengo, M. Tavakoli and P. Ullio, *Indirect Detection Analysis: Wino Dark Matter Case Study*, *JCAP* **07** (2014) 031 [arXiv:1401.6212] [INSPIRE].

[43] M. Baumgart, I.Z. Rothstein and V. Vaidya, *Constraints on Galactic Wino Densities from Gamma Ray Lines*, *JHEP* **04** (2015) 106 [arXiv:1412.8698] [INSPIRE].

[44] M. Cirelli, T. Hambye, P. Panci, F. Sala and M. Taoso, *Gamma ray tests of Minimal Dark Matter*, *JCAP* **10** (2015) 026 [arXiv:1507.05519] [INSPIRE].

[45] M. Beneke, A. Bharucha, A. Hryczuk, S. Recksiegel and P. Ruiz-Femenia, *The last refuge of mixed wino-Higgsino dark matter*, *JHEP* **01** (2017) 002 [arXiv:1611.00804] [INSPIRE].

[46] M. Baumgart et al., *Resummed Photon Spectra for WIMP Annihilation*, *JHEP* **03** (2018) 117 [arXiv:1712.07656] [INSPIRE].

[47] M. Beneke, *Perturbative heavy quark-anti-quark systems*, hep-ph/9911490 [INSPIRE].

[48] S. Kim and M. Laine, *Rapid thermal co-annihilation through bound states in QCD*, *JHEP* **07** (2016) 143 [arXiv:1602.08105] [INSPIRE].

[49] S. Kim and M. Laine, *On thermal corrections to near-threshold annihilation*, *JCAP* **01** (2017) 013 [arXiv:1609.00474] [INSPIRE].

[50] S. Biondini and M. Laine, *Re-derived overclosure bound for the inert doublet model*, *JHEP* **08** (2017) 047 [arXiv:1706.01894] [INSPIRE].

[51] S. Biondini and M. Laine, *Thermal dark matter co-annihilating with a strongly interacting scalar*, *JHEP* **04** (2018) 072 [arXiv:1801.05821] [INSPIRE].

[52] E. Braaten, E. Johnson and H. Zhang, *Zero-range effective field theory for resonant wino dark matter. Part I. Framework*, *JHEP* **11** (2017) 108 [arXiv:1706.02253] [INSPIRE].

[53] E. Braaten, E. Johnson and H. Zhang, *Zero-range effective field theory for resonant wino dark matter. Part II. Coulomb resummation*, *JHEP* **02** (2018) 150 [arXiv:1708.07155] [INSPIRE].

[54] E. Braaten, E. Johnson and H. Zhang, *Zero-range effective field theory for resonant wino dark matter. Part III. Annihilation effects*, *JHEP* **05** (2018) 062 [arXiv:1712.07142] [INSPIRE].

[55] A. Mitridate, M. Redi, J. Smirnov and A. Strumia, *Cosmological Implications of Dark Matter Bound States*, *JCAP* **05** (2017) 006 [arXiv:1702.01141] [INSPIRE].

[56] W.-Y. Keung, I. Low and Y. Zhang, *Reappraisal of dark matter co-annihilating with a top or bottom partner*, *Phys. Rev.* **D 96** (2017) 015008 [arXiv:1703.02977] [INSPIRE].

[57] K. Petraki, M. Postma and M. Wiechers, *Dark-matter bound states from Feynman diagrams*, *JHEP* **06** (2015) 128 [arXiv:1505.00109] [INSPIRE].

JHEP07(2018)096

[58] J. Harz and K. Petraki, *Higgs Enhancement for the Dark Matter Relic Density*, *Phys. Rev.* **D 97** (2018) 075041 [arXiv:1711.03552] [INSPIRE].

[59] J. Harz and K. Petraki, in preparation.

[60] M. Geller, S. Iwamoto, G. Lee, Y. Shadmi and O. Telem, *Dark quarkonium formation in the early universe*, *JHEP* **06** (2018) 135 [arXiv:1802.07720] [INSPIRE].

[61] N. Brambilla, M.A. Escobedo, J. Ghiglieri and A. Vairo, *Thermal width and gluo-dissociation of quarkonium in pNRQCD*, *JHEP* **12** (2011) 116 [arXiv:1109.5826] [INSPIRE].

[62] C. Itzykson and J. Zuber, *Quantum field theory*, McGraw-Hill (1980) [INSPIRE].

[63] Y. Kats and M.D. Schwartz, *Annihilation decays of bound states at the LHC*, *JHEP* **04** (2010) 016 [arXiv:0912.0526] [INSPIRE].

[64] A.D. Sakharov, *Interaction of an Electron and Positron in Pair Production*, *Zh. Eksp. Teor. Fiz.* **18** (1948) 631 [INSPIRE].

[65] A. Sommerfeld, *Über die Beugung und Bremsung der Elektronen*, *Annalen Phys.* **403** (1931) 257.

[66] P.R. Manuel Drees, Rohini Godbole, *Theory and Phenomenology of Sparticles*, World Scientific (2005).

[67] J. Edsjo and P. Gondolo, *Neutralino relic density including coannihilations*, *Phys. Rev.* **D 56** (1997) 1879 [hep-ph/9704361] [INSPIRE].

[68] S. El Hedri, A. Kaminska and M. de Vries, *A Sommerfeld Toolbox for Colored Dark Sectors*, *Eur. Phys. J.* **C 77** (2017) 622 [arXiv:1612.02825] [INSPIRE].

[69] S. Cassel, *Sommerfeld factor for arbitrary partial wave processes*, *J. Phys.* **G 37** (2010) 105009 [arXiv:0903.5307] [INSPIRE].

[70] S. Biondini, *Bound-state effects for dark matter with Higgs-like mediators*, *JHEP* **06** (2018) 104 [arXiv:1805.00353] [INSPIRE].

[71] A. Messiah, *Quantum mechanics*, North-Holland Pub. Co. (1962).

[72] A.I. Akhiezer and N.P. Merenkov, *The theory of lepton bound-state production*, *J. Phys.* **B 29** (1996) 2135.

[73] A.V. Manohar and I.W. Stewart, *Running of the heavy quark production current and 1/v potential in QCD*, *Phys. Rev.* **D 63** (2001) 054004 [hep-ph/0003107] [INSPIRE].

[74] A.V. Manohar and I.W. Stewart, *Renormalization group analysis of the QCD quark potential to order v^2*, *Phys. Rev.* **D 62** (2000) 014033 [hep-ph/9912226] [INSPIRE].

[75] J.J. Sakurai, *Modern quantum mechanics*, Addison-Wesley (1994).

[76] A. Pineda and J. Soto, *Effective field theory for ultrasoft momenta in NRQCD and NRQED*, *Nucl. Phys. Proc. Suppl.* **64** (1998) 428 [hep-ph/9707481] [INSPIRE].

[77] M.E. Luke, A.V. Manohar and I.Z. Rothstein, *Renormalization group scaling in nonrelativistic QCD*, *Phys. Rev.* **D 61** (2000) 074025 [hep-ph/9910209] [INSPIRE].

[78] B. Ioffe and M. Shifman, *At the Frontier of Particle Physics: Handbook of QCD: Boris Ioffe Festschrift*. vol. 4, World Scientific (2001).

[79] A.H. Hoang and M. Stahlhofen, *Ultrasoft NLL Running of the Nonrelativistic $O(v)$ QCD Quark Potential*, *JHEP* **06** (2011) 088 [arXiv:1102.0269] [INSPIRE].

JHEP07(2018)096